Time-resolved, 3D, laser-induced fluorescence measurements of fine-structure passive scalar mixing in a tubular reactor

E. Van Vliet, S. M. Van Bergen, J. J. Derksen, L. M. Portela, H. E. A. Van den Akker

Abstract A three-dimensional, time-resolved, laser-induced fluorescence (3D-LIF) technique was developed to measure the turbulent (liquid-liquid) mixing of a conserved passive scalar in the wake of an injector inserted perpendicularly into a tubular reactor with Re=4,000. In this technique, a horizontal laser sheet was traversed in its normal direction through the measurement section. Three-dimensional scalar fields were reconstructed from the 2D images captured at consecutive, closely spaced levels by means of a high-speed CCD camera. The ultimate goal of the measurements was to assess the downstream development of the 3D scalar fields (in terms of the full scalar gradient vector field and its associated scalar energy dissipation rate) in an industrial flow with significant advection velocity. As a result of this advection velocity, the measured 3D scalar field is artificially "skewed" during a scan period. A method to correct for this skewing was developed, tested and applied. Analysis of the results show consistent physical behaviour.

List of symbols

A	Deformation tensor
D_t, D_f	Reactor and injector diameter
L_x, L_y, L_z	Dimensions of the 3D-LIF measurement volume
N_x, N_y, N_z	Number of data samples per measurement volume
Re_m	Reynolds number based on mean velocity
Sc	Schmidt number
f	Focal length
$f_{c,lens}$, $f_{c,array}$	Cut-off frequency for camera lens and sensor array
f_θ, f_ϕ	Marginal probability density function for θ and ϕ
$f_{\theta\phi}$	Joint probability density function of θ and ϕ
Δt	Temporal separation of the 2D data planes
ΔT	Temporal resolution of the measurement volume
Δx, Δy, Δz	Spatial resolution of the measurement volume
γ, α	Deformation angle and deformation, where $\alpha=\tan\gamma$
ε	Fluid energy dissipation rate
λ_v, λ_Γ	Strain limited vorticity and scalar diffusion layers
ζ	Scalar concentration
η, η_B	Kolmogorov and Batchelor length scale
θ, ϕ	Spherical angles of the scalar gradient vector, $\nabla\zeta$
v	Kinematic viscosity
σ_e^{-2}	Half-thickness ($1/e^2$) of the laser sheet
τ, τ_a	Kolmogorov and Kolmogorov advection time scales
χ	Scalar energy dissipation rate
Γ	Scalar diffusivity
2D, 3D	Two- and three-dimensional
DNS	Direct numerical simulation
LIF	Laser-induced fluorescence
SED	Scalar energy dissipation rate
TR	Tubular reactor

© Springer-Verlag 2004

E. Van Vliet (✉), S. M. Van Bergen, J. J. Derksen, L. M. Portela
H. E. A. Van den Akker
Kramers Laboratorium voor Fysische Technologie,
Faculty of Applied Sciences, Delft University of Technology,
Prins Bernhardlaan 6, 2628 BW, Delft, The Netherlands
E-mail: eelco@klft.tn.tudelft.nl

1
Introduction

The mixing of initially segregated fluids represents a broad range of engineering problems. In many applications in process industries, reactants are dissolved in fluids. To bring about chemical reactions, the scalar components first have to be brought into contact on a molecular scale. Commonly in liquids, molecular mixing takes place on scales smaller than the smallest turbulent flow scales. As the reaction yield and the production of unwanted side products may strongly depend on the molecular mixing rate, modelling of turbulent reacting flows requires a sound understanding and description of the fine-scale mixing process. Three-dimensional measurement of the scalar concentration field is preferable, since both statistical (pdf) models (e.g. Fox 1997; Colucci et al. 1998; Van Vliet et al. 2001) and deterministic (mechanistic micro-mixing) models (e.g. Baldyga and Bourne 1984; Bakker 1996; Bakker and Van den Akker 1996) require orientation-dependant information, such as the scalar concentration gradient vector field, or the deformation rate of scalar layers.

For a given velocity field, the behaviour of any conserved, passive scalar quantity $\zeta(\mathbf{x}, t)$ is described by the scalar advection-diffusion equation:

$$\left[\frac{\partial}{\partial t} + u \cdot \nabla - \Gamma\nabla^2\right]\zeta(x,t) = 0, \tag{1}$$

where the kinematic viscosity, v, and the scalar diffusivity, Γ, determine the dynamical behaviour of the system via the Reynolds number, $Re = u_l l/v$ (with u_l and l being some characteristic velocity and length scale), and the Schmidt number $Sc = v/\Gamma$. Mixing can be considered to be the dissipation of the scalar energy $\frac{1}{2}\zeta(x,t)$, analogous to the dissipation of fluid kinetic energy (with energy dissipation rate, ε). It is therefore intuitive to consider the transport equation of the scalar energy,

$$\left[\frac{\partial}{\partial t} + u \cdot \nabla - \Gamma\nabla^2\right]\frac{1}{2}\zeta^2 = -\Gamma\nabla\zeta \cdot \nabla\zeta. \tag{2}$$

The left-hand side describes the advection and diffusion of the quantity, $\frac{1}{2}\zeta^2$. Since the right-hand side is always negative, it can only diminish the scalar energy and, hence, can be interpreted as a scalar energy dissipation rate (SED), denoted by χ, and defined as

$$\chi \equiv \Gamma\nabla\zeta \cdot \nabla\zeta. \tag{3}$$

The fluid kinetic energy of the turbulent flow produced at large scales is dissipated into heat by the action of molecular viscosity at the smallest turbulent scales, characterised by the Kolmogorov length scale, $\eta = (v^3/\varepsilon)^{1/4}$, and the Kolmogorov time scale, $\tau = (v/\varepsilon)^{1/2}$ (for significant advection by the mean flow, $\bar{U}$, a smaller time scale can be the Kolmogorov advection time scale, $\tau_a = \eta/\bar{U}$). In a Kolmogorov eddy, the steepening of velocity gradients due to straining of the larger scales is balanced by the flattening of gradients due to viscosity. An analogous process can be recognised in the mixing of a passive scalar. The diffusivity, Γ, of a passive scalar dissolved in a fluid is generally much smaller than the molecular viscosity. This allows the smallest length scales by which scalar gradients can be sustained to be much smaller than the Kolmogorov scales. The smallest scalar length scale is known as the Batchelor length scale, η_B. The Batchelor scale can be interpreted as the diffusion length, $(\Gamma\tau)^{1/2}$, of a scalar within one Kolmogorov eddy lifetime, τ, and, hence, can be related to the Kolmogorov length scale according to $\eta_B \approx Sc^{-1/2}\eta$, with a proportionality constant of approximately one.

Instead of the Kolmogorov scale, sometimes the "strain limited vorticity diffusion layer", $\lambda_v \sim (v/S)^{1/2}$, is taken to be the smallest turbulent length scale where dissipation takes place (with S being the outer scale uniform strain rate), e.g. Dahm et al. 1990. The strain limited diffusion layer is proportional to the Kolmogorov scale $(\lambda_v \sim \eta)$[1] and is often related to the outer scale Reynolds number by

$\lambda_v/l = \Lambda Re^{-3/4}$, with a constant, Λ, that lies in the range 5–25 (Su and Clemens 1999). The "strain limited scalar diffusion layer", λ_Γ, scales as $\lambda_\Gamma \approx Sc^{-1/2}\lambda_v$, with a proportionality constant of approximately one (similar to the Batchelor scaling). The interpretation of the Kolmogorov and Batchelor scale vs the strain limited vorticity and scalar diffusion layers is equivalent. In the design of our 3D-LIF experimental setup, we estimated the spatial and temporal resolution on the basis of the Kolmogorov and Batchelor scales, since these are directly related to the local energy dissipation. This choice is validated in Sect. 4.

In stochastic pdf models of turbulent reacting flows, the scalar energy dissipation rate plays a key role. Closure of the scalar transport equations, Eqs. 1 and 2, is often established by assumptions based on the SED induced by the numerically unresolved sub-grid scales. Therefore, measurements of the scalar energy dissipation are essential for model development and validation. Since the scalar energy is dissipated at the Batchelor scale, measurement of the scalar gradient field, $\nabla\zeta(x, t)$, and the associated scalar energy dissipation, χ, requires highly resolved determination of the scalar quantity in all three spatial dimensions, which becomes possible with the development of advanced optical laser techniques combined with the increasing capabilities of high-speed CCD cameras.

The imaging of a 3D scalar field can be achieved via two different approaches. The first involves the simultaneous imaging of the 2D scalar field using multiple closely spaced laser sheets (Frank et al. 1991; Landenfeld et al. 1998; Su and Clemens 1999; Nygren et al. 2002). In this method, there is no temporal delay between the imaging of the planes and, therefore, a true, non-skewed, 3D scalar field is obtained, which can be used to calculate the 3D scalar gradient field and its associated scalar energy dissipation rate in a single plane in the flow. One drawback of this method is that more than one camera is required so different scattering methods have to be used to discriminate between the signals from the planes. Moreover, it is not possible to extend the measurement of a 3D scalar gradient vector field in a 2D plane to a 3D data volume. This extension is necessary if measurements are to be used as a visualisation tool for the 3D scalar field to detect coherence of structures in the third dimension.

The second approach for 3D imaging employs a single sheet of laser light that is swept along the normal direction to obtain consecutive, closely spaced 2D images from which a (quasi-)3D concentration field is reconstructed (Yip and Long 1986; Yip et al. 1987; Prasad and Sreenivasan 1990; Dahm et al. 1991; Maas et al. 1994; Knaus et al. 1999; Hoffmann et al. 2002). With this method, the number of images in the normal direction is not restricted and, therefore, it is suitable for obtaining the visualisation of 3D structures in all three spatial directions. The drawback, however, is that the images within one 3D data volume are separated temporally. The time spacing between the consecutive planar concentration fields should, therefore, be much smaller than the smallest turbulent time scale, i.e. the minimum of the Kolmogorov time scale and the Kolmogorov advection time scale.

The quasi-3D-LIF technique (from here on referred to as 3D-LIF) was employed by Prasad and Sreenivasan

---

[1]For isotropic turbulence, both the strain rate, S, and the energy dissipation, ε, can be related to the Taylor micro scale, λ_g, by $S^2 = 2u_l^2/\lambda_g^2$ and $\varepsilon = 15vu_l^2/\lambda_g^2$ (Hinze 1975). Elimination of u_l/λ_g yields $S^2 = 2\varepsilon/(15v)$, which, in combination with $\lambda_v = c_1(v/S)^{1/2}$, leads to $\lambda_v = (c_1 15v^3/(2\varepsilon))^{1/4} \sim \eta$.

(1990) to investigate the mixing of a turbulent jet in water at a spatial resolution that was about four times the Kolmogorov scale. Dahm et al. (1991) and Maas et al. (1994) successfully measured the 3D scalar field in a similar flow facility at a spatial and temporal resolution that was adequate to resolve even the Batchelor scale. All of these measurements have in common a turbulent jet that was used to mix the measured scalar quantity. For the turbulent jet, momentum conservation implies that the product of the local length scale, l, and the velocity scale, u_l, is independent of the downstream distance, x, and that the length and velocity scale vary according to $l \sim x$ and $u_l \sim x^{-1}$, respectively. As a result, for a given Reynolds number, a large local macro length scale combined with, in principle, an arbitrarily low local advection velocity can be obtained. Consequently, the small-scale turbulent structures can be chosen to be relatively large, since these are proportional to the macro scales in a ratio depending on the Reynolds number only. By measuring far downstream of the injector, large macro scales are formed that are slowly advected with the centre line velocity of the jet, resulting in a Kolmogorov advection time scale comparable to, or even larger than, the Kolmogorov time scale.

In the present work, the aim is to extend the applicability of the 3D-LIF technique to measure the mixing in the more complex flow of an industrially applied tubular reactor with a perpendicular injector at $Re=4,000$. These reactors are commonly used in process industries, such as polymer production. Again, a turbulent jet is formed by the injector but, apart from that, an advection velocity is maintained by the main flow in the reactor. As a result, in contrast to the free jet flow, the fine-scale turbulent structures are advected at a considerable velocity by the mean flow. On top of that, the Kolmogorov length scales are relatively small for the given Reynolds number since the macro length scales are limited by the size of the reactor diameter. These complications put higher demands on the temporal and spatial resolution of the measuring system, and imply the need for special measures to correct the skewing of the measured concentration field. We use a high-speed CCD camera that is capable of capturing 955 frames per second at a spatial resolution of 256×256 8-bit pixels. As the short exposure time must be compensated for by a high intensity of illumination to keep an adequate signal-to-noise ratio of the fluorescent signal captured by the CCD camera, a 25 W (all lines) continuous Argon-ion laser was used, which is an improvement over the 5 W laser used in the work presented previously in Van Vliet et al. (2000a; 2000b).

In spite of the high temporal resolution achieved, an artificial deformation (skewing) of the measured 3D concentration field is observed. By means of a direct numerical simulation (DNS) of scalar mixing in an isotropic turbulent flow, it is demonstrated that the observed deformation in the measurements can be related to an artificial shear caused by the mean advection during a single realisation of a 3D scalar field. Since the mean advection velocity can be estimated from the cross-correlation function evaluated from consecutive 3D data volumes, a correction to this artificial skewing is applied by using the instantaneous advection velocity.

A generic description of the 3D-LIF technique is given in Sect. 2, the characteristic length and time scales of the turbulent flow are estimated (Sect. 2.1) and compared to the spatial and temporal resolution (Sect. 2.3) of the 3D-LIF optical configuration described in Sect. 2.2. In Sect. 3, the skewing effect of a large advection velocity is studied and a correction method is proposed. The results will be presented in Sect. 4.

First, emphasis is put on the visualisation of the huge amount of data acquired with the 3D-LIF setup. A more quantitative description of the data is in the form of distribution functions of the concentration and the scalar energy dissipation field that can be obtained from such 3D data sets. This quantitative data is used to study the downstream development of the mixing scalar field in the tubular reactor. Finally, in Sect. 5, a retrospective of the results is given, and some concluding remarks are made.

2
The experimental setup

2.1
The flow facility

The flow facility reactor (Fig. 1) consists of a Perspex tube (internal diameter D_t =0.10 m) in which a steady, moderately turbulent flow of water is established, with a mean velocity of U_m=0.04 m/s. A perpendicular feed pipe with an external diameter D_f=0.02 m is inserted a distance of $0.75D_t$ into the reactor. The injector opening of D_i=2 mm in diameter is located at the centre line of the reactor. The ratio between the dye feed velocity and the main stream velocity is approximately 10. The small internal dye feed opening makes the momentum contribution of the dye relatively small. It is hence expected that: (1) closely downstream from the injector, mixing is enhanced by the combined effect of the turbulence generated by both the wake and the jet, and (2) further downstream, the turbulence induced by the wake is dominant. The Reynolds numbers based on the mean velocity and the internal reactor diameter, D_t, and the external injector diameter, D_f, are $Re_m \approx 4,000$ and $Re_f \approx 800$, respectively. The Reynolds number based on the jet velocity and feed opening diameter, D_i, is $Re_i \approx 800$.

An estimate of the smallest turbulent length and time scales is required to assess the spatial and temporal resolution of the experimental setup for the given flow conditions. A rough estimate can be made using the undisturbed flow in a straight pipe with circular cross section. For $Re=4,000$, the centre line energy dissipation is about 3×10^{-6} m^{2}s^{-3} (Van Vliet et al. 2000b) which, in combination with a kinematic viscosity of $\nu=1.0 \times 10^{-6}$ m^{2}s^{-1}, leads to a Kolmogorov length scale, $\eta \approx 0.8$ mm, and a Kolmogorov time scale, $\tau \approx 0.6$ s. In our flow facility, the mean velocity of 0.04 m/s, combined with the Kolmogorov length scale of 0.8 mm, leads to a Kolmogorov advection time scale of 20 ms. The Schmidt number of the fluorescent dye used in the experiment (a disodium Fluorescein solution) is $Sc \approx 2,000$ (Walker 1987), yielding a Batcelor scale of $\eta_B = Sc^{-1/2}\eta \approx 20 \ \mu$m.
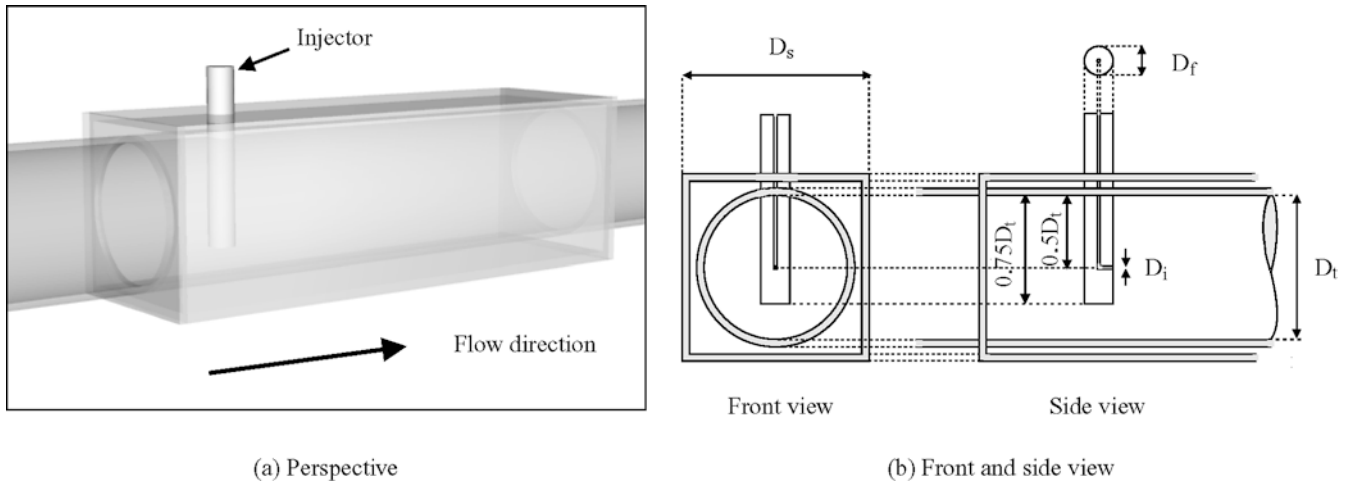
(a) Perspective

(b) Front and side view

Fig. 1a, b. Perspective (**a**) and schematic (**b**) representation of the tubular reactor at the position of the injector. The internal reactor diameter, D_t, the external injector diameter, D_f, and the injector feed opening, D_i, are 0.10 m, 0.02 m and 2 mm, respectively. To reduce image deformations due to the cylindrically shaped tube wall, a square transparent box filled with water was installed around the tube

2.2
Optical and electronics arrangement

An overview of the experimental setup is given in Fig. 2. As a light source, an Argon-ion laser (Spectra-Physics, BeamLok 2080) was used. Only the blue line (λ=488.0 nm) continuously emitting 8 W was employed. The laser beam was widened into a horizontal sheet by a negative cylindrical lens (f=−6.35 mm, Melles Griot 01 LCN 000). This sheet was swept in the normal direction by a low-inertia galvano mirror (GSI Lumonics, G-120DT) with its axis of rotation in the focal point of the cylindrical lens (see Fig. 3). A function generator (Exact Electronics Inc., model 505A) yielded the asymmetric triangle wave that was used to slave the angle of the galvano mirror. In this way, the galvano mirror traversed the laser sheet downward through the measuring volume on the shallow slope of the triangle wave and re-positioned the sheet to its initial top position on the steep slope. During the re-positioning of the sheet, one or two (depending on the height of the measuring volume) spurious frames were captured, which had to be removed afterwards.

The height of the measuring volume could be adjusted by setting an appropriate triangle wave amplitude. By means of a custom-built controller unit, two pulse trains in the appropriate ratio were generated, and these triggered the CCD camera and the function generator. The number of frames within one measuring volume was set by the ratio between the triangle wave frequency and the CCD camera frame rate.

The positive spherical lens (f=500 mm, Melles Griot) placed at its focal distance from the galvano mirror (as illustrated in Fig. 3) had three purposes. First, since the galvano mirror was positioned in the focal point of the spherical lens, the scanning laser sheet leaving the mirror at an angle was converted by the spherical lens into a sheet that was swept parallel to its normal direction. This is required to obtain a uniformly sampled data volume in the sheet normal direction at the measuring plane. Second, since the focal point of the cylindrical lens also coincided with the galvano mirror, the widening sheet was converted into a parallel sheet. In this way, the (1/e)-width in terms
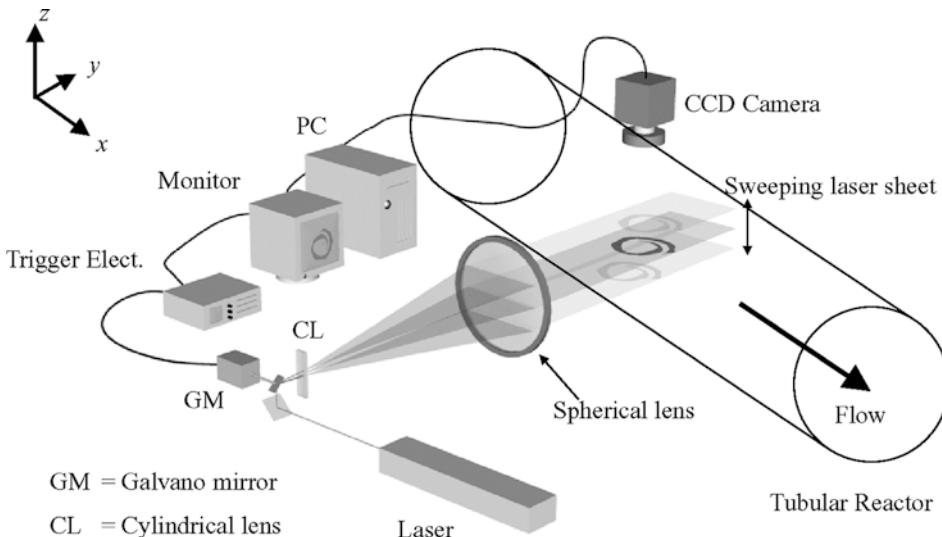

Fig. 2. Overview of the key elements of the experimental setup, consisting of a laser illumination source, sheet forming optics, a high-speed digital CCD camera, a PC to capture the measurement data and some electronics to slave the galvano mirror used to sweep the laser sheet in the depth direction. The reference axes show the coordinate system used, with the origin at the injector opening located at the centre line
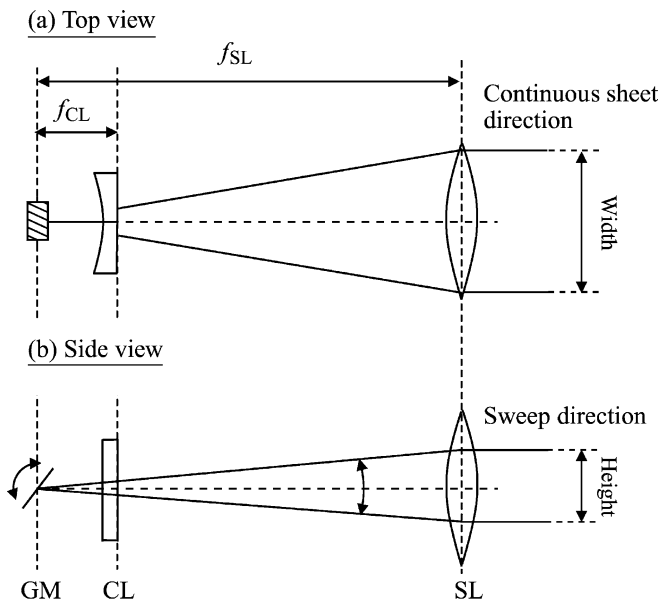
GM = Galvano mirror
CL = Cylindrical lens

(a) Top view

(b) Side view

Fig. 3a, b. Schematic representation (not to scale) of top (**a**) and side (**b**) view of the optical arrangement of the galvano mirror (*GM*), cylindrical lens (*CL*) and spherical lens (*SL*). The focal points of the negative cylindrical lens ($f_{CL}=-6.35$ mm) and the positive spherical lens ($f_{SL}=500$ mm) coincide at the galvano mirror to create a data volume parallel in both the continuous sheet and the sweep directions

of the centre line intensity of the laser sheet was set to be about 170 mm.[2] Since the width of the measuring volume (25 mm) was much smaller than the sheet width, the Gaussian intensity profile of the laser sheet exhibits a decay of smaller than 2% over the spanwise sheet direction and, hence, intensity was considered uniform over the measuring volume. A uniform sheet intensity is important when the concentration is to be measured from the emitted fluorescent light. Finally, the spherical lens was used to focus the waist position of the laser sheet at the measuring position in the reactor. With the optical configuration used, the beam waist based on the ($1/e^2$) decay was about 200 μm at the measuring position. The sheet thickness variation over the measuring position was less than 1%.

The light emitted from the dye is imaged by means of a high-speed digital CCD camera (Dalsa CA-D6–0256) positioned above the TR with its optical axis perpendicular to the laser sheet. The 55 mm lens (Nikon, Micro Nikkor 1:2.8–32) mounted on the camera was equipped with a low-pass optical filter (Melles Griot, GC495) with its optical cut-off at 495 nm in order to separate the 518 nm fluorescent signal from the elastically scattered 488 nm laser light. The CCD camera captured 955 frames per second on a light-sensitive area of 256×256 pixels. Each single pixel represents the fluorescence intensity in 256 levels of grey values (1 byte/pixel). The scalar concentration was obtained from the fluorescence intensity since the two are proportional in the low-dye concentration limit. The data stream of about 60 Mb/s was stored in the RAM

---

[2] In the present article, the width of a laser sheet will be based on the ($1/e$) intensity decay position, while the thickness will be based on the ($1/e^2$) position. The definitions are in a ratio of $\sqrt{2}$.
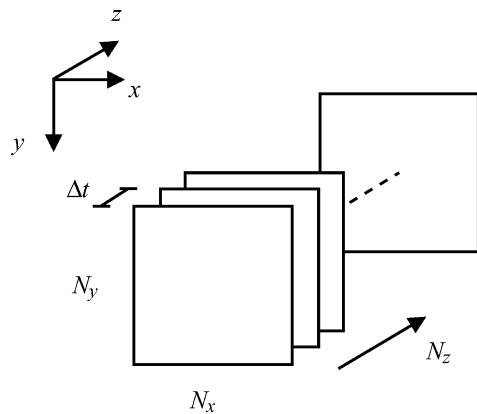
(a) Data volume from consecutive planes
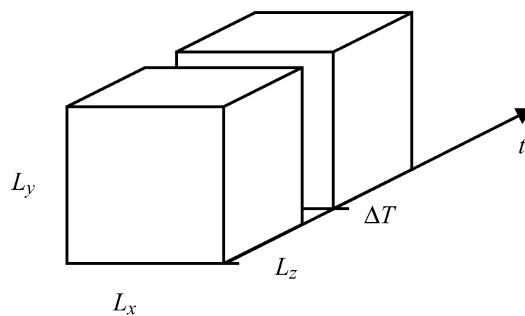
(b) Consecutive data volumes in time

Fig. 4. a Schematic representation of a data volume consisting of N_z closely spaced data planes of $N_p \times N_p$ pixels each. **b** The (4D) data space consisting of (3D) data volumes captured successively in time, mapping the conserved scalar concentration field in the $L_x \times L_y \times L_z$ volume in object space. The data volumes are sampled at a temporal resolution ΔT on a $N_p \times N_p \times N_z$ grid of $\Delta x \times \Delta y \times \Delta z$ sample volumes

of an NT workstation. As 1 GB of memory was available, measurement series of up to 15 seconds could be performed.

2.3
Spatial and temporal resolution

Figure 4a represents a 3D data volume comprising of N_z planes in the normal direction, each consisting of $N_x \times N_y$ data points in the spanwise directions. The resolution of the data samples ($\Delta x \times \Delta y \times \Delta z$) in the $N_x \times N_y \times N_z$ data volume is determined by the CCD camera optics in the spanwise direction and the inter-planar distance in the normal direction. The resolutions, Δx and Δy, within each spatial data plane can, in principle, be made very high by increasing the magnification of the CCD camera optics.

The resolution, Δz, in the normal direction is limited by the thickness of the laser sheet. The average laser sheet cannot be made arbitrarily thin, since it is limited by the Rayleigh range of the laser beam. Ideally, no overlap exists between two adjacent image planes in a data volume; if, however, the overlap is small, and the time Δt between the successive planes in a single data volume is small enough

such that the scalar field can be considered frozen, the measured scalar field is the result of the true scalar field convoluted with the sheet profile.

Dahm et al. 1991 showed that a de-convolution with the *known* Gaussian beam profile can be applied to correct for the beam profile convolution to some extent, hereby, allowing some overlap between adjacent laser sheets. In their measurements, the inter-plane separation was $\Delta z = 220$ μ m and the $(1/e)$-thickness of the laser sheet was given to be 380 µm (corresponding to a $\sqrt{2} \times 380$ μ m $= 537$ μ m$(1/e^2)$-thickness). The fraction of energy of the laser sheet that was in the range $-\Delta z/2 < z < \Delta z/2$ is given by

$$\left(\frac{\pi}{2}\sigma_{e^{-2}}^2\right)^{-1/2}\int_{-\Delta z/2}^{\Delta z/2} e^{\left(-2s^2/\sigma_{e^{-2}}^2\right)}\mathrm{d}s = \mathrm{erf}\left(\frac{1}{2}\sqrt{2}\Delta z/\sigma_{e^{-2}}\right),$$

(4)

where $\sigma_{e^{-2}}$ is half the $(1/e^2)$-thickness of the laser sheet. As a result, a thickness of $\sigma_{e^{-2}} = 537/2 = 269$ μ m combined with a sample spacing of $\Delta z = 220$ μ m led to a fraction, 0.59, of the total sheet energy that was inside the sample plane, while the adjacent sheet overlapped by a fraction of almost 0.21 each. In the present measurements, the sheet's half-thickness of $\sigma_{e^{-2}} = 100$ μ m is about equal to the inter-plane distance, Δz. As a result, a fraction of 0.68 of the total energy is inside the sample plane, while a fraction of 0.16 of the energy overlaps the adjacent planes at each side (as illustrated in Fig. 5). The overlap with the next
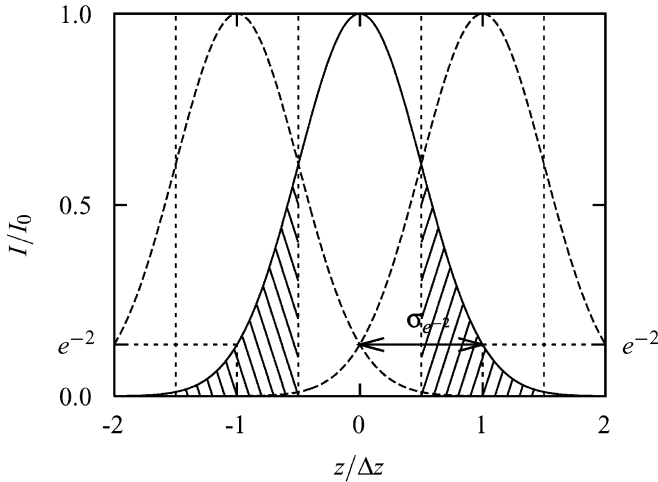
nearest neighbours is ignored since it was less than 1%, hence, the effect of the Gaussian sheet profile is approximated to be the convolution of the 3D data volume with a cubic $(3\times3\times3)$ matrix with the only non-zero coefficients in the sheet normal direction to be 0.16, 0.68 ,and 0.16. The de-convolution of the measured scalar field was performed in the Fourier domain by multiplying the Fourier transformed measured scalar field with the inverse Fourier transformed convolution matrix. The spatial resolution of the back-transform to the physical domain is now also 100 µm in the sheet normal direction.

The spatial resolution in the spanwise sheet directions is set equal to the resolution in the normal direction by adjusting the CCD camera optics. The image sensor of the CCD camera consists of 256×256 pixels of size l_p=10 µm. The magnification (defined as the ratio $m = l_p/\Delta x$) is set to be m=0.1 by adjusting the 55-mm lens mounted on the CCD camera. As a result, the imaging resolution in the spanwise sheet directions is set to be 100 µm, yielding a sample volume of $\Delta x \times \Delta y \times \Delta z = 100^3$ μ m^3 (cases II and III in Table 1). Also, measurements with a coarser spatial resolution of 400^3 µm^{3}are gathered to obtain a macroscopic view of the 3D turbulent jet downstream of the injector (case I, Table 1).

The size of the x–y plane is fixed by the number of pixels of the image sensor of the CCD camera to be $N_x\Delta x = N_y\Delta y = 25.6$ mm in each direction for the high-resolution measurements. The size of the data volume in the depth direction depends on the number of data planes, N_z, according to $L_z = N_z\Delta z$. Choosing a large number of data planes improves the range of length scales resolved in the depth direction. A trade-off exists, however, between using this range and the temporal resolution, ΔT, to acquire the data volumes. Increasing N_z degrades the temporal resolution according to $\Delta T = N_z/f_{\mathrm{CCD}}$, with f_{CCD} being the camera frame rate of 955 fps. For visualisation purposes, the number of data planes per volume is chosen to be as large as 41, giving L_z=4.1 mm combined with a temporal resolution of $\Delta T = 42.9$ ms. Determining the scalar energy dissipation requires only three data planes. Since the last data plane from every measurement volume is spurious, somewhat more planes are taken to be sure that enough sharp images are captured within each data volume. In our case, N_z is chosen to be 10, giving a depth of the data volume of L_z=1.0 mm combined with a temporal resolution of 10.5 ms.

The spatial resolution of the measurement system estimated so far is an upper limit; only the pixel spacing, l_p, of the sensor array was taken into account in determining the array-limited cut-off frequency, $f_{\mathrm{c,array}}$=1/(2l_p). Since the image plane moves with respect to the camera,

Fig. 5. Illustration of three adjacent laser sheet profiles that overlap in the normal direction. In the present experiment, $\sigma_{e^{-2}}$ is equal to the inter-plane distance Δz, resulting in an overlap between the adjacent laser sheets, indicated by the *hatched areas*

Table 1 The spatial and temporal dimensions and resolution of our 3D-LIF setup compared to the flow characteristics given in Table 2

Case	N_z	Δx, Δy		Δz		$L_{x,y}$		L_z		ΔT		Δt	
		µm	η_B	µm	η_B	mm	η	mm	η	ms	η/U	ms	η_B/U
I	40	400	20	400	20	102.4	128	16	20	41.9	21.0	1.05	2.1
II	41	100	5	120	6	25.6	32	4.9	6.1	42.9	2.1	1.05	2.1
III	10	100	5	100	5	25.6	32	1.0	1.3	10.5	0.5	1.05	2.1

the cut-off frequency set by the limited depth of view of the camera should also be considered. This is done by introducing the diffraction-limited cut-off frequency, $f_{c,lens}$ (Hopkins 1955):

$$f_{c,lens} = 1.22\frac{f_{\#}(1+m)}{m^2\delta}, \qquad (5)$$

where δ is the focusing error (the absolute distance between the actual and the "in-focus" object plane), and $f_{\#}$ is the aperture number of the lens (i.e. the ratio of the focal length and the aperture diameter of the lens, f/d). Choosing a large aperture number, $f_{\#}$, improves $f_{c,lens}$, but it also limits the light captured by the optical system by a factor proportional to $f_{\#}^2$ and, hence, degrades the signal-to-noise ratio. The spatial resolution and the signal quality are well balanced when the array-limited and diffraction-limited cut-off frequencies are approximately equal (Paul et al. 1990). For the maximum focusing distance given as $\delta=L_z/2$, this yields an expression for the f-number in terms of magnification, m, pixel-to-pixel distance, l_p, and the depth of the measuring volume, L_z:

$$f_{\#} = 0.20\frac{m^2 L_z}{(1+m)l_p}. \qquad (6)$$

Equation 6 is a good guideline for choosing the aperture number such that the sample resolution in the object plane is achieved over the whole depth-of-view of the data volume without unnecessarily limiting the light-gathering ability of the lens. In our case III ($m=0.1, l_p=10$ μm and $L_z=10$ mm), it implies that $f_{\#} \approx 1.8$.

Due to the shorter focal distance of the waist-forming spherical lens and the higher frame rate of the CCD camera (955 fps vs 140 fps), the spatial and temporal resolutions of our experimental setup ($\Delta x = 100$ μm and $\Delta t = 10.5$ ms), are higher than the resolutions achieved with a similar setup by Dahm et al. (1990) where $\Delta x = 220$ μm and $\Delta t = 45$ ms. In terms of the smallest turbulent length and time scales, however, our resolution turns out to be worse. In Table 1, the spatial and temporal resolutions and dimensions for the three different optical configurations are compared to the turbulent flow scales given in Table 2. The macro measurements of case I were performed on a coarse resolution in order to create a measurement volume large enough to visualise the whole turbulent jet downstream of the injector. The resolution of both cases II and III was chosen to be as small as possibly allowed by the minimum laser sheet thickness in order to resolve the smallest turbulent scales. The resulting resolution was about 5 Batchelor length scales (or 0.11 Kolmogorov length scales).

Table 2. Main characteristics of the turbulent flow

Reynolds number	Re	4,000
Mean velocity (ms^{-1})	U_c	0.04
Kolmogorov length scale (m)	η	0.8×10^{-3}
Bachelor length scale (m)	η_B	20×10^{-6}
Kolmogorov time scale (s)	τ	0.6
Advection time scale (s)	τ_a	20×10^{-3}
Kinematic viscosity (m^{2}s^{-1})	ν	1.0×10^{-6}

For two reasons, we expect that the spatial resolution is sufficiently close to the Batchelor scale to allow for estimating the scalar energy dissipation field. First, the estimate of the Batchelor scale is based on the equilibrium between the scalar energy flux and dissipation and, hence, represents an order of magnitude of a whole range of dissipative length scales. The resolution of 5 Batchelor scales may be sufficiently fine to at least resolve part of the small-scale dissipation field. On top of that, it was mentioned in the introduction (Sect. 1) that there is no consensus on the proportionality constant of the Batchelor scales, and we have opted for the most stringent one. Secondly, the measured scalar field is low-pass-filtered by the area-averaging effect of the CCD pixels in the sheet spanwise directions and by the convolution effect of the Gaussian sheet profile in the sheet normal direction. This at least prevents aliasing effects due to the non-resolved high-frequency components, and a smoothed, but non-erroneous, gradient vector is obtained from the 3D scalar data field.

2.4
Measurement procedure

The number of data volumes that could be captured per measurement by the 1.0 GB of memory was limited to 955. Consequently, it was not possible to measure for a period longer than 15 seconds, or about six macro time scales (which are estimated to be about $T = D_t/\bar{U} = 2.5$ s. To improve the statistical accuracy of the results, a time gap of 0.5 s was introduced between every three successive data volumes. This way, within a three-block succession, the 3D data volumes were still accessible on the highest temporal resolution of $\Delta t = 10.5$ ms. This procedure increased the measurement time to more than 70 macro time scales, but assumes statistical independence between the data volumes.

Next to the fluorescent signal, each image consists of a background signal due to (elastically) scattered laser light and a dark signal due to several camera noise contributions. The combined background and dark images can be measured independently of the signal in the tubular reactor operating without fluorescent dye being injected. To correct for these combined dark and background images, it is subtracted from each data plane afterwards.

The laser power and f-number of the collecting camera optics were kept constant over all of the measurements presented. After subtraction of the combined background and dark signal, the measured laser intensity was normalised with the intensity of the non-mixed dye of concentration, ζ_0, directly at the outlet of the injector. This intensity was set equal to the camera saturation grey value of 256, such that the full signal range of 256 grey values was employed. Since the temporal fluctuating noise contribution (which cannot be corrected for) of the camera was given to be about 1 grey value, the signal-to-noise ratio (SNR) varies in the range 1–255. As a result, concentration values no lower than about $0.004\zeta_0$ could be measured.

The de-convolution filter to correct for the overlap of the Gaussian beam profile in the sheet normal direction was applied (Sect. 2.3). This way, a spatial resolution of

100 µm in both the normal and spanwise sheet directions was achieved. To reduce the spatial noise contribution, the spatial resolution was slightly degraded by a 3×3×3 cubical Gaussian filter with a standard deviation of one grid spacing in all directions.

The concentration gradient vector field was obtained from the 3D data set by means of a central difference scheme. The associated scalar energy dissipation, $\chi = \Gamma \nabla \zeta \cdot \nabla \zeta$, was normalised with a measurement for the maximum scalar energy dissipation that can be estimated from the given initial concentration and smallest turbulent scalar length scale: $\chi_0 = \Gamma(\zeta_0/\eta_B)^2$. The figures presenting the scalar energy dissipation will show the square root, $\chi^{1/2}$, of the scalar energy dissipation, i.e. the modulus of the scalar gradient vector, $|\nabla \zeta|/(\zeta_0/\eta_B)$.

3
Skew correction procedure

It was mentioned in the introduction that skewing of the measured concentration field, due to the mean advection during a single realisation, is a potential problem of the 3D-LIF technique, since an artificial (macro) shear is induced, which affects the micro-scales of the scalar field. In this section, a correction procedure is proposed, which uses the instantaneous mean advection velocity over a 3D data volume (estimated by means of a cross-correlation technique) to compensate for this artificial shear by imposing an equal shear in the opposite direction.

A passive scalar mixing in homogeneous isotropic turbulence was used to study the effect of the artificial shear and to test the correction procedure. In Fig. 6a, the scalar concentration, $\zeta(\mathbf{x})$, on a 128×128×16 slab extracted from a single realisation of the DNS is shown. The coordinate axes and the associated spherical angles are defined in Fig. 7a.

For an isotropic turbulent flow field, the concentration gradient vectors are homogeneously distributed over the 4π solid angle. An infinitesimal surface element in spherical coordinates varies according to $r^2 \sin(\theta)\mathrm{d}\theta\mathrm{d}\phi$, resulting in a joint probability density function (joint pdf) of the spherical angles, given by
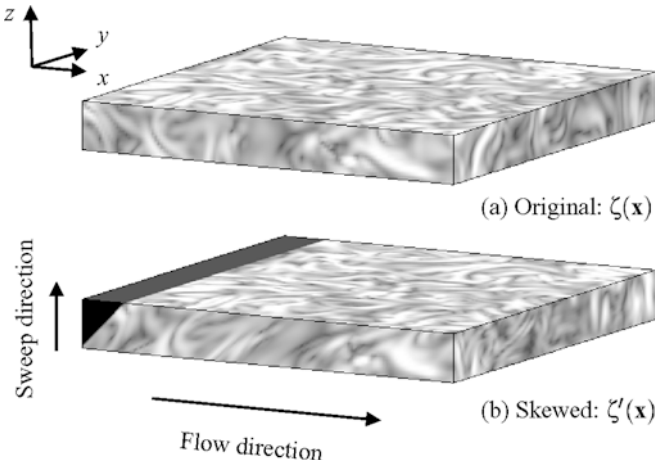
$$f_{\theta\phi}(\theta, \phi) = \sin(\theta)/4\pi. \tag{7}$$

After integration, the marginal pdfs of θ and ϕ are found to be:

$$f_\theta(\theta) = \int_0^{2\pi} f_{\theta\phi}(\theta, \phi')\mathrm{d}\phi' = \frac{1}{2}\sin(\theta) \tag{8}$$

and

$$f_\phi(\phi) = \int_0^\pi f_{\theta\phi}(\theta', \phi)\mathrm{d}\theta' = \frac{1}{2\pi}, \tag{9}$$

respectively. To represent the 2D joint pdf by a 3D surface, the measured joint pdf is normalised according to

$$f_{\theta\phi}^*(\theta, \phi) = 4\pi f_{\theta\phi}(\theta, \phi)/\sin\theta, \tag{10}$$

and the 3D surface is formed by the spherical coordinates (r, θ, ϕ), with $r \sim f_{\theta\phi}^*$. In Eq. 10, a homogeneous distribution of the concentration gradient vectors over the 4π solid angle space leads to a value of $f_{\theta\phi}^* = 1$ and, consequently, a sphere with constant radius $r=1$ is obtained. Deviations of the vector density from the homogeneous distribution are reflected by deformation of the sphere surface.

The distribution of the concentration gradient vectors over the spherical angles is represented by the joint pdf, $f_{\theta\phi}$, shown in Fig. 8a. The joint pdf is evaluated from 50 independent DNS realisations of a scalar mixing into an isotropic homogeneous turbulent flow. The marginal pdfs, f_θ and f_ϕ, are depicted next to and above the joint pdf, respectively, and compared to the marginal pdfs of a homogeneous distribution of gradient vectors given by Eqs. 8 and 9. The gradient vector field of the isotropic DNS data is shown to be almost completely homogeneously distributed over the 4π solid angle. The 3D representation of the joint pdf (after transformation with Eq. 10) is depicted in Fig. 9a. The homogeneous distribution is now reflected by the almost perfect spherical shape of the surface.

For a significant advection, the concentration field, $\zeta(\mathbf{x})$, can no longer be considered "frozen" during a single realisation, so a skewed concentration field, $\zeta'(\mathbf{x})$, may be
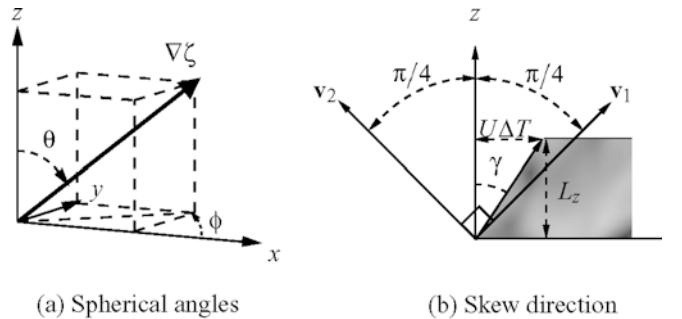

Fig. 6. **a** Concentration field, $\zeta(\mathbf{x})$, on a 128×128×16 grid extracted from a 128×128×128 DNS grid. **b** Concentration field, $\zeta'(\mathbf{x})$, obtained after artificially skewing the DNS data using Eqs. 11, 12, 13, and 14. A mean flow in the positive x direction, combined with a sweeping laser sheet in the positive z direction is assumed

Fig. 7. **a** Definition of the spherical angles with respect to the coordinate axes. The azimuthal angle, ϕ, represents the angular distance in the x–y plane from the positive x axis with $0 \leq \phi \leq 2\pi$, and the elevation, θ, is the angular distance from the positive z axis with $0 \leq \theta \leq \pi$. **b** Side view of the skewed concentration field of Fig. 6b, showing the deformation angle, $\gamma = \arctan(U\Delta T/L_z)$. The eigenvectors, $\mathbf{v}_1$ and $\mathbf{v}_2$, indicate the principal directions of expansion and compression, respectively
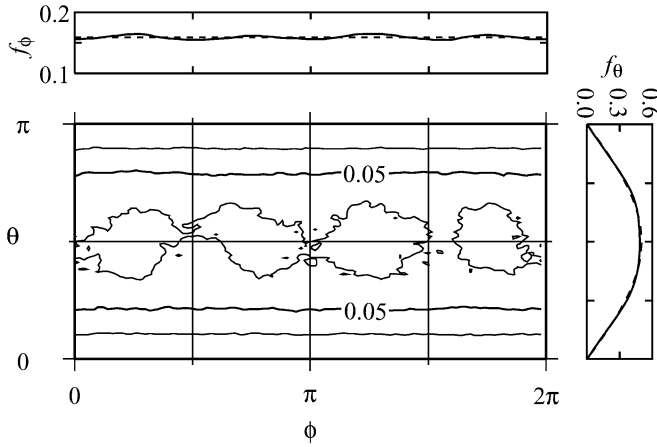
(a) Original
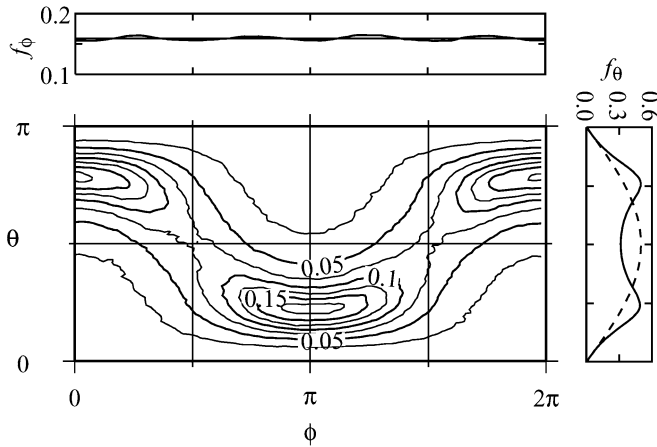
(b) Skewed ($\alpha = 1$)
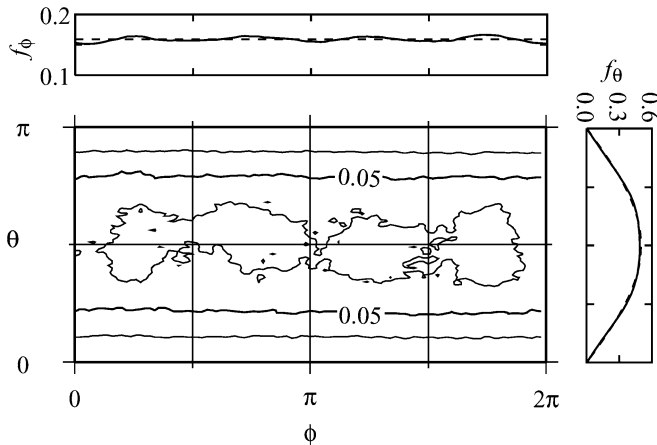
(c) Corrected

Fig. 8a–c. Influence of the skewing of the concentration field on the joint pdf, $f_{\theta\phi}$, of the spherical angles. The marginal pdfs, f_θ and f_ϕ, are displayed next to and above each joint pdf, respectively, and compared to the pdfs belonging to the homogeneous distribution of gradients vectors given by the *dashed lines*. The joint pdf of the original data is shown in **a**. The artificial skew applied to the concentration field leads to a clear deviation of the joint pdf in **b**. After the skew correction, the original joint pdf is recovered **c**. The small differences between the joint pdfs of the original and corrected data can be attributed to interpolation round-off errors of the pixel filling algorithm applied to skew the data
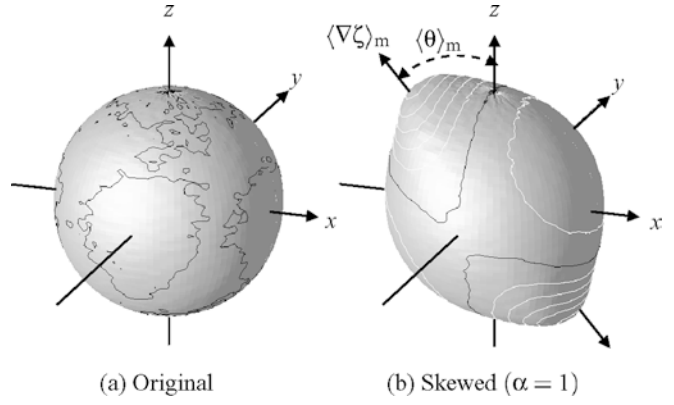
(a) Original   (b) Skewed ($\alpha = 1$)

Fig. 9a, b. Distribution over the 4π solid angle of the concentration gradient vectors of the original (**a**) and skewed (**b**) concentration field, corresponding to the 2D joint pdf shown in Fig. 8a, b, respectively. *White lines* are used to indicated every 0.5 iso-contour level, except for the unity level (corresponding to the homogeneous distribution with $r=1$), which is indicated by the black iso-contour

measured instead. Assuming only deformation of the concentration fields due to the mean advection velocity, the skewed concentration field can be written as a linear transformation of the original concentration field. This is a reasonable assumption in our case, since the Kolmogorov advection time scale is estimated to be about 30 times smaller than the Kolmogorov time scale (see Sect. 2.1). Hence, we model the skewing of the concentration field by means of the relation

$$\zeta'(x') = \zeta(x), \tag{11}$$

where

$$x' = x + \delta x \tag{12}$$

and

$$\delta x = Ax \Leftrightarrow \begin{bmatrix} \delta x \\ \delta y \\ \delta z \end{bmatrix} = \begin{bmatrix} 0 & 0 & \alpha \\ 0 & 0 & 0 \\ 0 & 0 & 0 \end{bmatrix} \cdot \begin{bmatrix} x \\ y \\ z \end{bmatrix}. \tag{13}$$

The tensor, A, applies a pure shear with a deformation given by the parameter, α. The deformation angle, $\gamma=\arctan\alpha$ (depicted in Fig. 7b), is related to the mean velocity in the positive x direction according to

$$\tan\gamma = \frac{U\Delta T}{L_z}. \tag{14}$$

Equations 11, 12, 13 and 14 are applied to skew the DNS concentration field shown in Fig. 6a by using a pixel filling algorithm (Castleman, 1979)[3]. A mean advection velocity of 16 grid cells per DNS realisation ($\Delta T = 1$) is imposed, which, in combination with the height of a data volume of 16 grid points, leads to a deformation of $\alpha=1.0$.

---

[3]For every discrete grid position, $\mathbf{x}'$, of the output concentration field, ζ', the value is retrieved from the input concentration field, ζ, at the corresponding position, $\mathbf{x}$, given by Eqs 12 and 13. Since $\mathbf{x}$ is generally located within the fixed grid, a bi-linear interpolation is applied using the values at the eight surrounding grid points to estimate $\zeta(\mathbf{x})$.

The resulting skewed concentration field is depicted in Fig. 6b. The joint pdf of the spherical angles is depicted in Fig. 8 and the 3D representation in Fig. 9. A clear deviation from the isotropic distribution of Fig. 8a is found. In the 3D representation, the skewing of the concentration field leads to a preferential direction along $\langle \nabla \zeta \rangle_m$, located in the x–z plane at an angle of $\langle \theta \rangle_m$.

The skewing of the concentration field can be better understood by decomposing A into a symmetrical and an anti-symmetrical part:

$$A = A^{(s)} + A^{(a)} = \begin{bmatrix} 0 & 0 & \alpha/2 \\ 0 & 0 & 0 \\ \alpha/2 & 0 & 0 \end{bmatrix} + \begin{bmatrix} 0 & 0 & \alpha/2 \\ 0 & 0 & 0 \\ -\alpha/2 & 0 & 0 \end{bmatrix}.$$
(15)

The symmetrical part, $A^{(s)}$, yields the principal deformations $\alpha/2$, $-\alpha/2$ and 0, acting along the principal axes of $A^{(s)}$, given by the unit vectors $v_1 = (1, 0, 1)/\sqrt{2}$, $v_2 = (-1, 0, 1)/\sqrt{2}$ and $v_3 = (0, 1, 0)/\sqrt{2}$, respectively. Figure 7b shows the eigenvectors, v_1 and v_2, at an angle of $\pi/4$ with respect to the z axis. The concentration field is purely expanded and compressed in the v_1 and v_2 directions, respectively. Since the eigenvalue of v_3 is zero, no deformation occurs in the direction of the y axis. In addition to the pure compression–expansion due to $A^{(s)}$, a rotation along the y axis is applied by the anti-symmetrical part, $A^{(a)}$. For small α, the angle of rotation can be considered to be proportional to α. In the limit of infinite shear, however, the anti-symmetrical part, $A^{(a)}$, will align the sheared concentration field to the shear angle, γ.

In Fig. 10, the mean gradient vector orientation $\langle \theta \rangle_m$ is plotted as a function of the shear angle, γ. For small shear angles, γ, the preferential direction, $\langle \theta \rangle_m$, is approaching $\pi/4$ along the eigenvector, v_2. For increasing shear, the anti-symmetrical part of the deformation tensor, A, starts to rotate the concentration field from $\pi/4$ towards the positive z axis (leading to smaller values of $\langle \theta \rangle_m$). When the shear angle is larger than $\pi/4$, the limit, $\langle \theta \rangle_m \to \pi/2 - \gamma$ (shown with the dashed line) is approached, meaning that the preferential direction of the concentration gradient vectors is perpendicular to the shear angle, γ. Based on Fig. 10, we suggest that the skew correction should only be applied for $\gamma = 0 \sim \pi/4$ since, for larger values, the 3D data field is affected too much by the anti-symmetrical part, $A^{(a)}$.

In Fig. 11, the effect of skewing on the scalar energy dissipation is shown. The long tail of the SED distribution of the original data is an indication of the intermittent behaviour of the mixing concentration field. The same result was found by Brethouwer (2001) who performed a DNS simulation of a scalar mixing on homogeneous isotropic turbulence on a $256\times256\times256$ computational grid. After skewing the concentration field with a deformation $\alpha=1$, an increased intermittency is observed as a result of the compression of the concentration field in the direction of the smallest eigenvalue. For scalar energy dissipation measurements, it is therefore necessary to apply a correction for the skewed concentration field.

For a known mean advection velocity, the same deformation tensor with a deformation rate of opposite
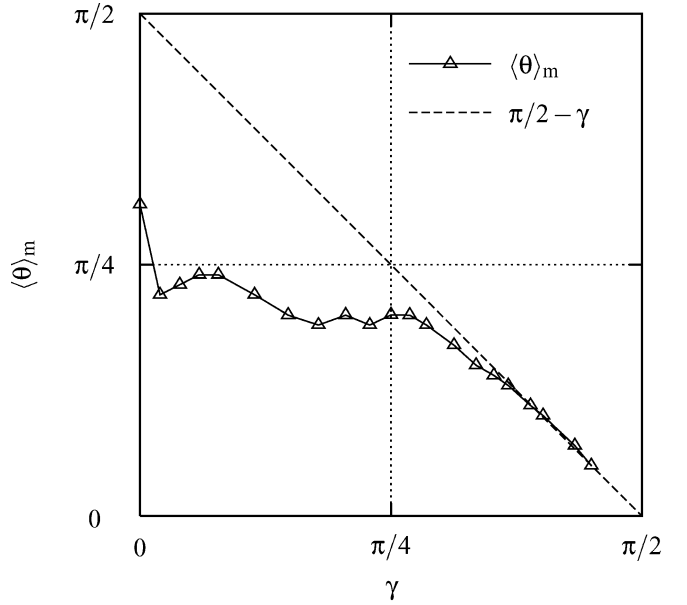

Fig. 10. Angle $\langle \theta \rangle_m$ of the preferential direction of the concentration gradient vector vs the shear angle, γ (see Fig. 7 for angle definitions)
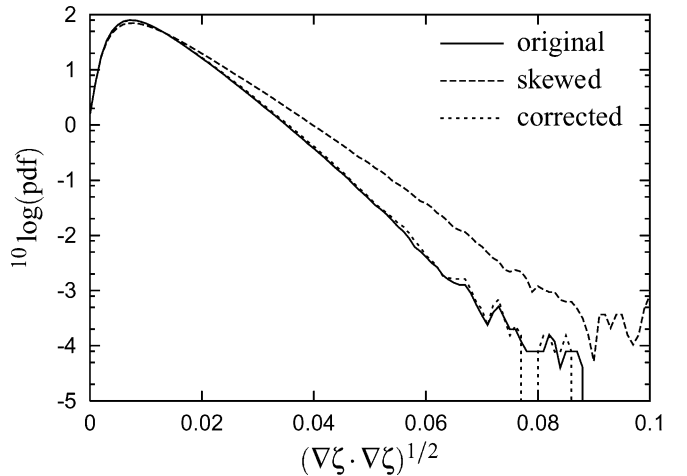

Fig. 11. Skewing of the concentration field increases the scalar energy dissipation rate. After the skew correction, the original distribution is recovered

sign to α promoted by the advection can be used to correct for the skewing. This correction was applied to the artificially skewed data. After the correction, the homogeneous vector distribution (Fig. 8) and the distribution of the energy dissipation (Fig. 11) are recovered almost completely. This shows that, for a known advection velocity, a correction to the skewing of the concentration field can be successfully applied.

In the artificially skewed data, the advection velocity was imposed, and the de-skewing tensor is available beforehand. If de-skewing is to be applied on 3D-LIF measurement data, however, a calculation for the velocity is not known, and an adequate estimate of the mean advection velocity has to be obtained from the measurement data themselves. The velocity can be estimated from the cross-correlation function of two successive data volumes. A uniform advection velocity in the x direction over

the entire data volume was assumed. The cross-correlation is obtained from the centre x–y planes extracted from the two subsequent 3D data volumes. The cross-correlation, $R(\mathbf{x}, t)$, is estimated using the conjugate multiplication of the Fourier transformed 2D image planes according to

$$R_\zeta(x, t) = F^{-1}\{F\{\zeta(x,t)\} \cdot F^*\{\zeta(x, t + \Delta T)\}\}, \qquad (16)$$

where F and F^{-1} represent the forward and backward Fourier transform operator, respectively, and the complex conjugate is indicated by the superscript, $*$. The mean displacement of the concentration field is obtained from the location of the correlation peak.

4
Results

In this section, the results obtained with the 3D-LIF setup are presented. Before going on to the quantitative analysis after Sect. 4.2, a 2D macro measurement is presented in Sect. 4.1 in order to get an insight into the global mean scalar transport downstream of the injector. In Sect. 4.2, some visualisations of the 3D data are evaluated to assess the spatial, temporal and signal resolution.

4.1
Two-dimensional macro measurements

The radially inserted injector complicates the flow field significantly. Large-scale flow structures are formed in its wake, and mixing is enhanced. To get an impression of the global, large-scale scalar transport downstream of the injector, a macro planar laser-induced fluorescence (PLIF) measurement was carried out in two centre planes; one parallel and one perpendicular to the feed pipe. Figure 12a shows the average dye concentration. The most striking effect is the upwardly moving dye plume due to the blockage promoted by the injector. From the side view, it appears that the dye continues to move upwards until the top of the reactor tube is reached at about $x=2D_t$. From there on, a clear separation of dye between the upper and lower regions over the full extent of the measuring section can be seen. The top view of Fig. 12a shows that the dye has left the horizontal centre plane after about one diameter, D_t, downstream of the feed pipe. After reaching the top of the reactor tube, the dye moves along the outer wall region downwards and re-enters the horizontal measuring plane at about $x=3D_t$. From this point, the dye is advected mainly along the tube walls.

A numerical simulation of the flow in the tubular reactor was performed to get a deeper insight in the velocity field that drives the large-scale scalar transport. Figure 12b shows the instantaneous velocity field obtained from a large eddy simulation performed on a numerical grid of 100×100×800 cells (Van Vliet et al. 2003). The Reynolds number of the main flow and the ratio of the jet velocity to the main velocity are taken as equal to the experimental conditions. Again, an upwardly inclined jet is observed, which quickly reaches the top of the reactor at about $1.5D_t$. Since the Fluorescein is transported by the jet, this numerical result agrees, at least qualitatively, with the macroscopic measurements.

4.2
Visualisation of the 3D data

A single realisation of the jet downstream of the injector measured with the 3D-LIF technique on a coarse resolution (case I, Table 1) is shown in Fig. 13. Due to the low spatial resolution, a relatively large area of the jet is visible. The smallest flow structures are not resolved and the scalar energy dissipation field should be considered as low-pass-filtered. The measurement illustrates, however, the development of the jet downstream of the injector, and shows the capability of the setup to obtain a "frozen" 3D image of the mixing dye. The upwardly inclined jet that was found with the 2D-LIF measurement shown in Fig. 12a is again observed; the dye fed at $z/D_t=0$ reaches the top plane of the measurement volume at $z/D_t=0.1$, while none of it reaches the bottom plane at $z/D_t=-0.04$.

An example of the 3D-LIF measurement at a high resolution, containing 40 frames per data volume is presented in Fig. 14. The 3D nature of the data is clearly illustrated by the continuity of the scalar structures over the edges of the data volume. The side planes, which are constructed from the consecutive closely spaced images, show similar vortical structures as the top plane, which is captured instantaneously as a single CCD image. This suggests that both the spatial resolution and the range of length scales in the depth direction are adequate, and that the flow field can be assumed as frozen during the time that the sheet scans the measuring volume. The square root of the normalised scalar dissipation, $(\chi/\chi_0)^{1/2}$, is shown at the faces of the data volume in Fig. 14b. Both the concentration and the scalar dissipation appear to occur in layer-like structures, which are randomly oriented with respect to the laser sheet.

The white box drawn in the front corner of the measurement volumes shown in Fig. 14 is enlarged in Fig. 15. The concentration isosurface (Fig. 15b) confirms that the dye structures at the outer faces of the measuring volume (Fig. 15a) are connected internally. Figure 15c shows that a smoothly varying gradient vector field can be derived from the scalar concentration. The scalar energy dissipation rate obtained from this vector field (Fig. 15d) shows that molecular mixing occurs in layer-like structures, which reveal much more fine-scale details than the concentration field. This agrees with the idea that, for high Sc mixing, the scalar gradient can be sustained on much smaller scales than the Kolmogorov scale (e.g. Dahm et al. 1990; Bakker and Van den Akker 1996; Brethouwer 2001).

Despite the relatively short distance from the injector, it appears that the concentration is significantly smaller than the initial concentration of the dye that was injected, and that the scalar structures are already quite smooth without a sharp definition. We expect that this can be attributed to the obstruction promoted by the injector, which had a significant influence on the macro scale transport downstream of the feed pipe (see Fig. 12). The upwardly inclined jet showed back-mixing and recirculation of dye was observed. At least part of the measured scalar structures may have had a residence time that is longer than that calculated from advection by the mean flow in a straight path from the feed pipe. It is likely that the effect
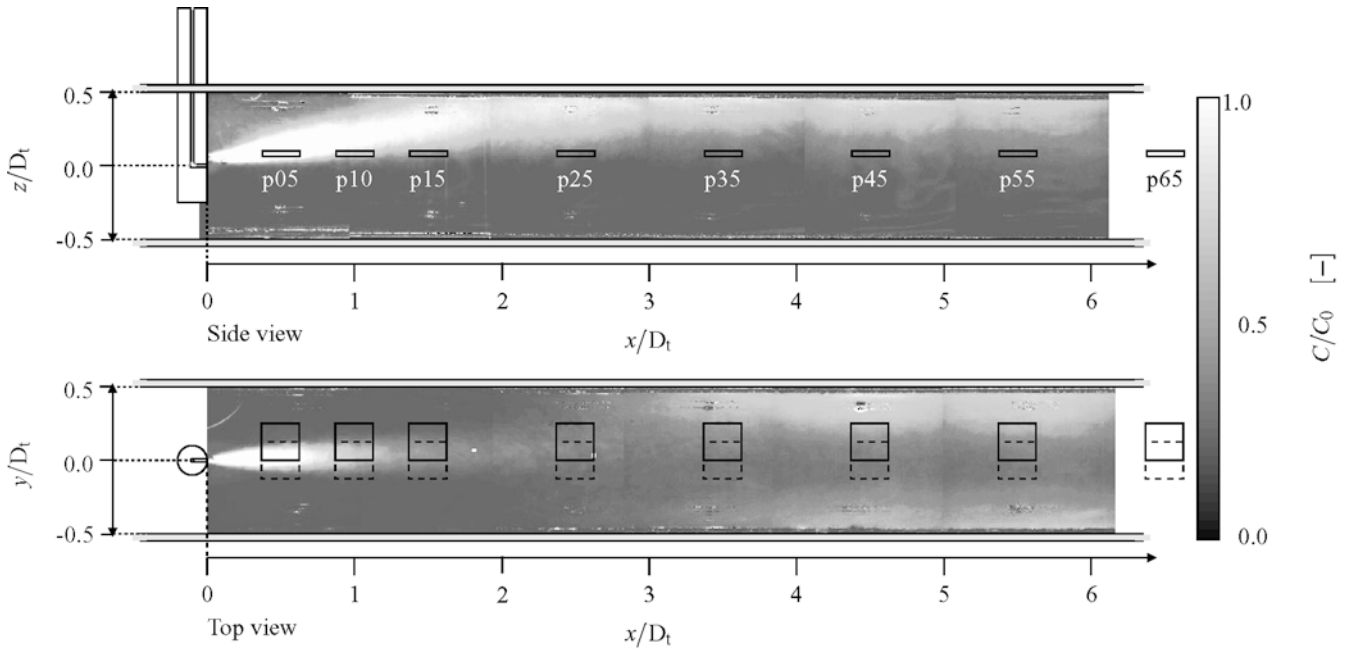
(a) Average dye concentration (experimental result)
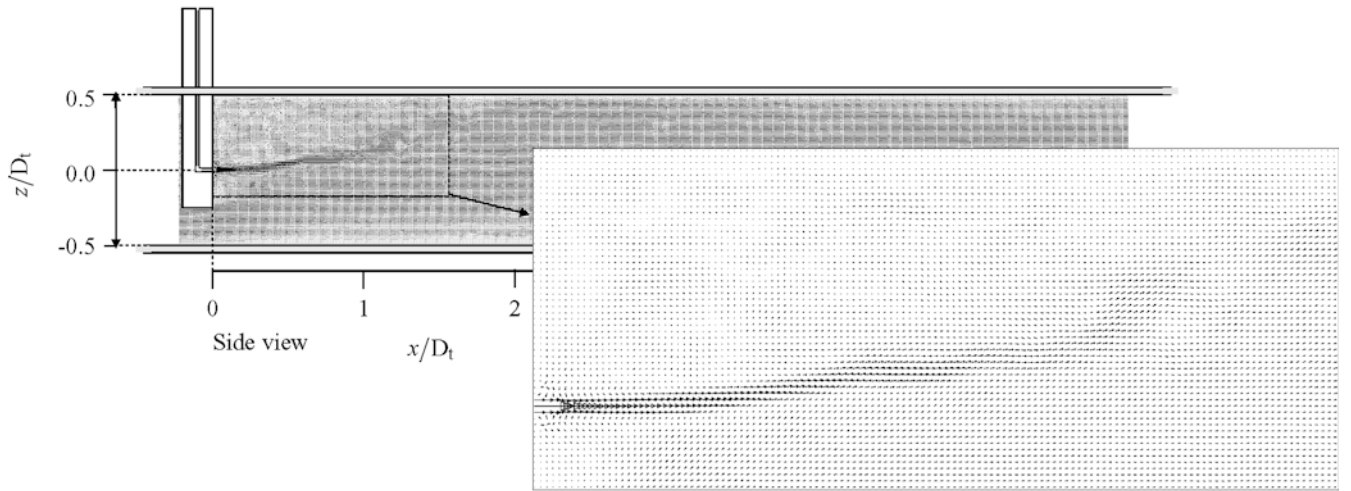
(b) Instantaneous velocity field (numerical simulation)

Fig. 12. a The average dye concentration obtained with a planar laser-induced fluorescence (PLIF) experiment in a centre plane parallel (*side view*) and perpendicular (*top view*) to the feed pipe. Each figure is actually formed from six separate PLIF measurements, each capturing the fluorescence signal at consecutive areas of $D_t \times D_t = 10 \times 10 cm^2$. The average concentration for each position was calculated from 256 independent images of 256×256 pixels.

The positions *p05–p65* indicate the size and position of the data volumes of the 3D-LIF micro-measurements presented in Sect. 4. **b** Instantaneous velocity field of the turbulent wake downstream of the injector, obtained with a large eddy simulation based on a lattice-Boltzmann scheme (Derksen and Van den Akker 1999). Both the experimental and the numerical results show that the wake behind the feed pipe causes the jet to move upward

of these complex downstream flow patterns is reflected on the scalar micro-scales by their diffuseness.

4.3
Analysis of a three-block sequence
Figure 16a, b shows the concentration and scalar energy dissipation over the centre planes extracted from three consecutive realisations of 3D data volumes (each con-

taining 10 frames) obtained at position p65 ($x=6.5D_t$, see Fig. 12) using the 3D-LIF configuration given by case III (Table 1). In Sect. 2.3, the temporal resolution of this case was estimated to be about $0.5\tau_a$, corresponding to about 0.07τ. The temporal resolution is adequate to resolve the small-scale fluctuations of the Kolmogorov eddies, which is reflected in the three-block sequence by the relatively small changes of dye structures in the consecutive
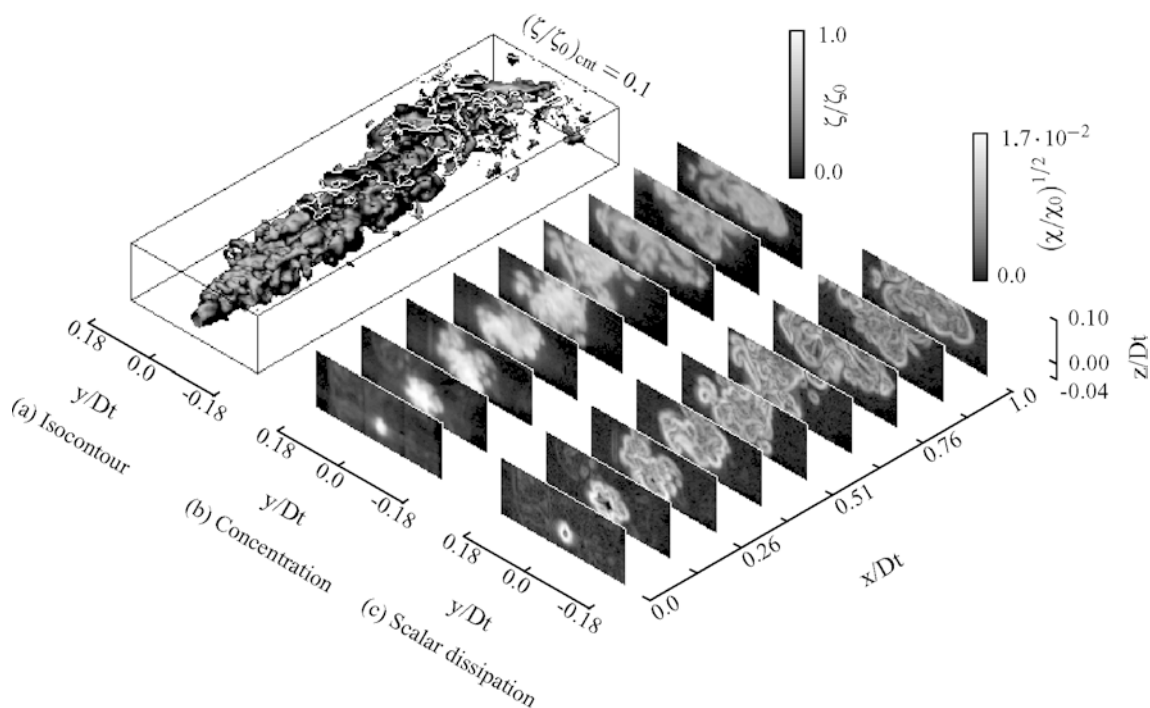
Fig. 13a–c. Single realisation of a 3D-LIF measurement on a coarse spatial resolution of the turbulent fluorescent jet downstream the injector.**a** An isosurface of the concentration field at a value of $\zeta/\zeta_0=0.1$.**b, c** The concentration and scalar energy dissipation field in nine consecutive planes normal to the flow direction. The coordinate axes (with respect to the injector inlet) are normalised with the internal reactor diameter, D_t
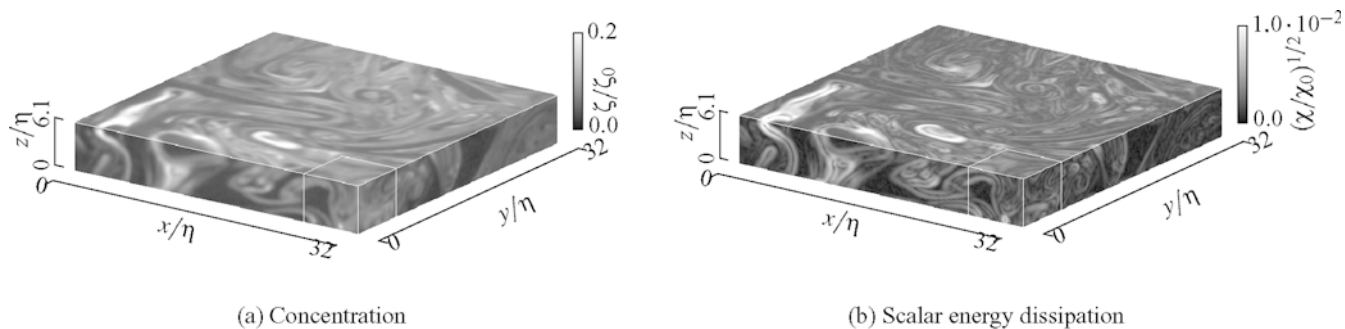

Fig. 14a, b. The concentration field (**a**) and the corresponding scalar energy dissipation rate field (**b**) obtained from a single realisation of the 3D-LIF measurement consisting of 256×256×40 data points carried out at position p15 at $x=1.5D_t$ downstream of the injector (see Fig. 12a). The spatial dimensions are normalised with the Kolmogorov length scale, η, given in Table 1. The *white box* in the right front corner is studied in detail in Fig. 15

realisations. The mean displacement of dye structures over the consecutive realisations of Fig. 16 can be obtained from the peak location in the cross-correlation function, which is evaluated using Eq. 16. The cross-correlation function evaluated from the first and second realisations is shown in Fig. 17. A Gaussian peak fit algorithm is used to estimate the peak location at 4.40±0.02 pixels in the streamwise, positive x direction. The displacement over the second and third realisations was found similarly to be 4.34±0.02 pixels. The mean velocity during the second realisation is estimated from the average displacement of 4.37±0.03 pixels to be 0.043±0.003 m/s. The displacement in the y direction is neglected since it was always smaller than 0.1 pixels and, hence, close to the noise level of the Gaussian peak algorithm.

The white box drawn in the second realisation with an area of 5×5 mm is shown in detail in Fig. 18. The dimensions of the characteristic eddy illustrated by the L_η arrows are of the order of the Kolmogorov length scales as estimated in Sect. 2. An idea of the diffusion length scale of the edge of the eddy is given by the arrow L_{η_B}. Compared to the Batchelor scale (which was estimated to be 40 times smaller than the Kolmogorov scale or five times smaller than the pixel resolution) the diffusion length is quite large; it has dimensions extending over about 10 pixels. The concentration profile along the horizontal line shows the same smooth variation extending over about 10 pixels or more (the image consists of 50^2 pixels). An image (at the same resolution) of a particle obtained from a focusing measurement is
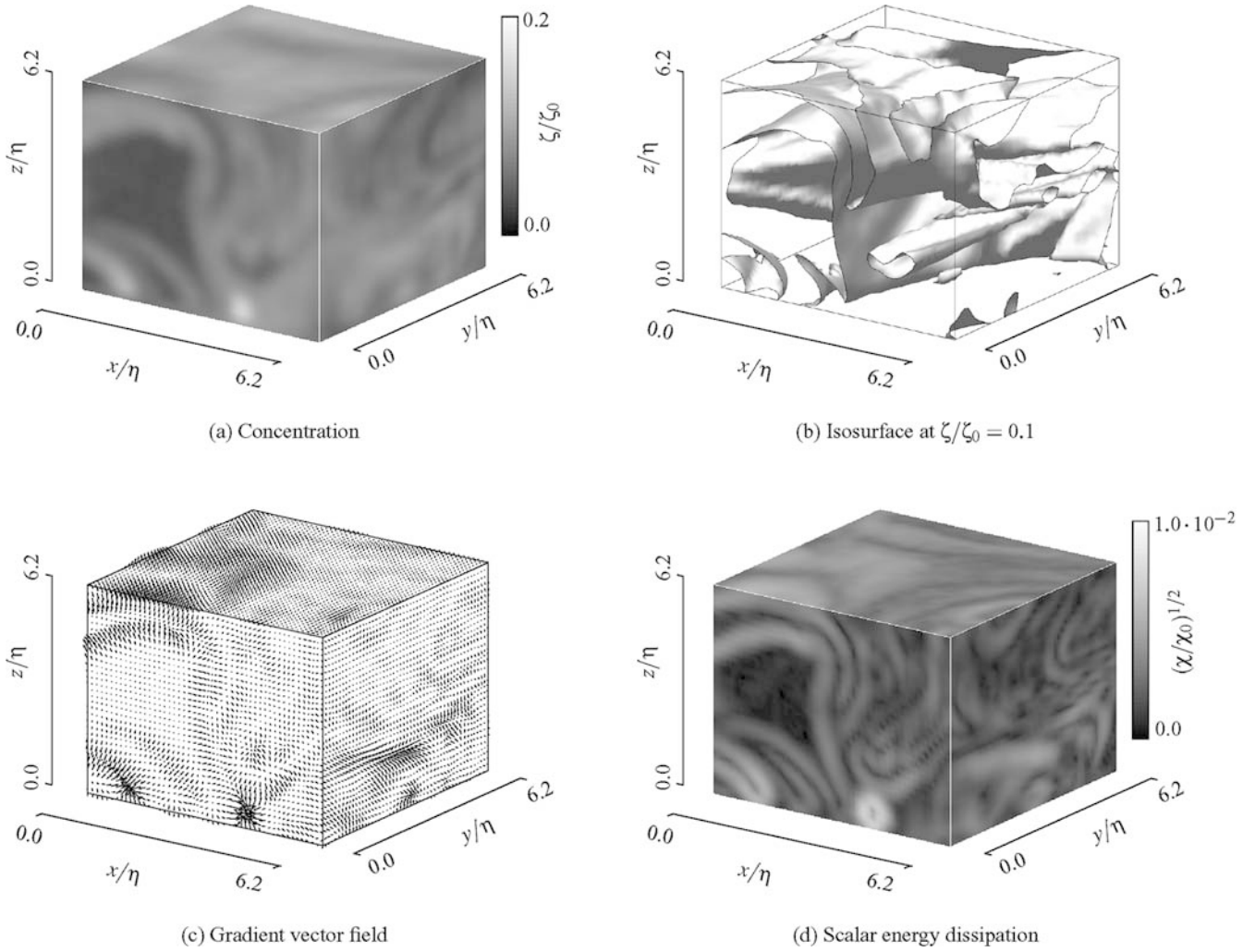
(a) Concentration

(b) Isosurface at $\zeta/\zeta_0 = 0.1$

(c) Gradient vector field

(d) Scalar energy dissipation

Fig. 15a–d. Enlargement of the 50×50×40 data point from the section indicated by the white box shown in Fig. 14. **a** Concentration over the outer faces of the section. **b** Concentration isosurface. **c** 3D vector gradient field derived from the scalar concentration. **d** Square root of the scalar energy dissipation

shown in the top left inset of the figure. These kind of particles (of size about 10 µm) were naturally present in the fluid flowing through the laser sheet, and were used to focus the camera (without the optical low-pass cut-off filter). The particle was imaged over 4 pixels, indicating that the image blur was comparable to the pixel resolution (as a result of Eq. 6). After application of the Gaussian filter, the edges of the particle extended over no more than 2 pixels, implying sharp images. Apparently, the edges of $L_\eta \approx 10$ cannot be related to resolution limits, and Kolmogorov-size scalar eddies can have a diffusion length larger than the Batchelor scale. A spatial central difference scheme can be applied in at least the major part of the concentration field. This is confirmed by the smoothly varying 2D projection of the resulting concentration gradient vector field, which is shown in Fig. 18b. The three individual gradient vector components along the horizontal line fluctuate at more or less similar intensity around zero, showing that all components contribute more or less equally to the total scalar energy dissipation.

4.4
Skew correction

In Sect. 3, it was shown that the mean velocity applies a pure shear on the measured 3D concentration field that effectively skews the data volume. As a result, the concentration field is compressed along the eigenvector, $\mathbf{v}_2$ (pointing to the upstream direction at $\theta=\pi/4$ from the z axis, see Fig. 7b). Consequently, the concentration gradient vector field is aligned with this eigenvector and its magnitude is increased, leading to an artificially increased scalar energy dissipation.

In Fig. 19a, the joint pdf of the spherical angles of the concentration gradient vector field is shown, derived from 325 independent realisations of 3D concentration data volumes measured at position p65 (x/D_t=6.5). The joint pdf shows a similar meandering deviation from the homogeneous distribution as found by the skewed DNS of Sect. 3. The meandering was found at all measuring positions.

Every measured data volume is de-skewed via Eqs. 11, 12, 13 and 14) using a deformation, $-\alpha$.
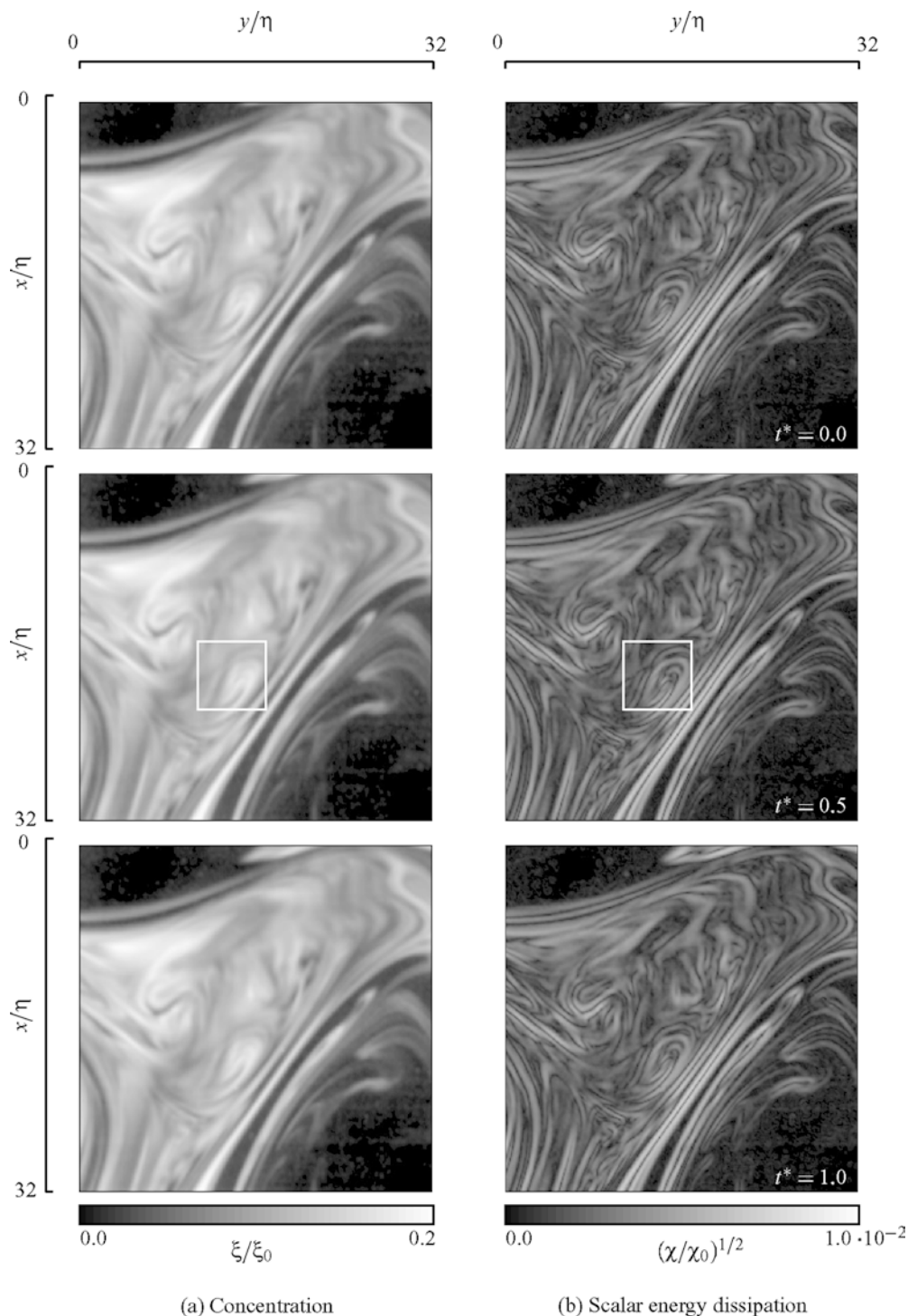
Fig. 16a, b. Evolution of the concentration field (**a**) and square root of the scalar energy dissipation field (**b**) over a centre plane extracted from successive realisations of 3D data volumes consisting of 10 layers. The time, $t^\star$, is normalised with the Kolmogorov advection time scale η/U. The positive $x$axis indicates the streamwise flow direction. The white square is enlarged in Fig. 18

In Fig. 19b, the joint pdf of the spherical angles obtained from the de-skewed data volumes is shown. The typical meandering deviation of the joint pdf is clearly reduced. The irregularities that were still found in the joint pdf could not be related to the artificial skew of the advection velocity. We assume that these are introduced by laser sheet fluctuations and measuring inaccuracies. It has to be emphasised that the estimate of the joint pdf of the spherical angle is very sensitive to small irregularities in the distribution of the spherical angle;

Dahm et al. (1991) found irregularities in their results of the spherical angle joint pdf of about the same order of magnitude.

The effect of the skew correction on the distribution of the scalar energy dissipation is shown in Fig. 20. The skew correction results in a decreased frequency of high values for the scalar energy dissipation (reflected by the lower tail of the tail of the pdf). This qualitatively corresponds to the behaviour of the SED obtained from the DNS results shown in Fig. 11.
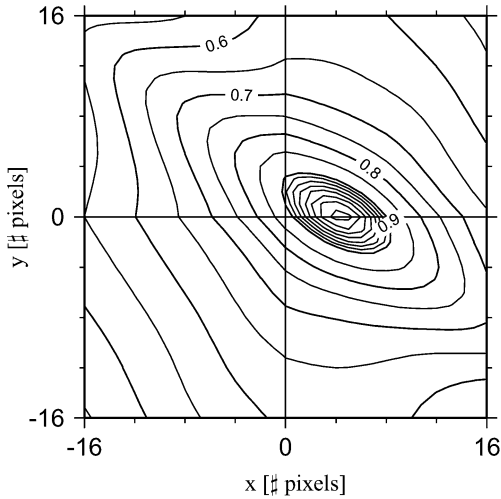
Fig. 17. Central part of the cross-correlation function of the first two realisations depicted in Fig. 16. The peak is shifted along the positive x axis due to the mean displacement of the concentration field in the streamwise direction. The inclined orientation of the isocontours corresponds to the direction of the layers in the concentration field itself

4.5
Analysis of the scalar energy dissipation distribution

The pdf depicted in Fig. 20 shows a high probability of measuring small values for the scalar energy dissipation, whilst the wide, more or less exponentially decaying tail toward the high values indicates that the high scalar energy dissipation is a less frequently occurring, rare event. This behaviour is generally found for turbulent scalar mixing (Brethouwer 2001; Overholt and Pope 1996; Dahm et al. 1991) and reflects the intermittent behaviour of the scalar energy dissipation field. To capture its intermittent behaviour, the logarithm of the SED is often studied and it is commonly assumed that the SED is log normally distributed (Kolmogorov 1962).

In Fig. 21, the pdf of $\log_{10}(\chi/\chi_0)$ is shown by the solid lines for near and far downstream positions. Both figures show a bi-modal distribution. In the near downstream position, a clear separation of both peaks exists, while in the far downstream position, the right peak tends to merge into the left one. Since the left, low-SED-value peak virtually remains in the same position in both graphs, it is likely that this peak is associated with the noise
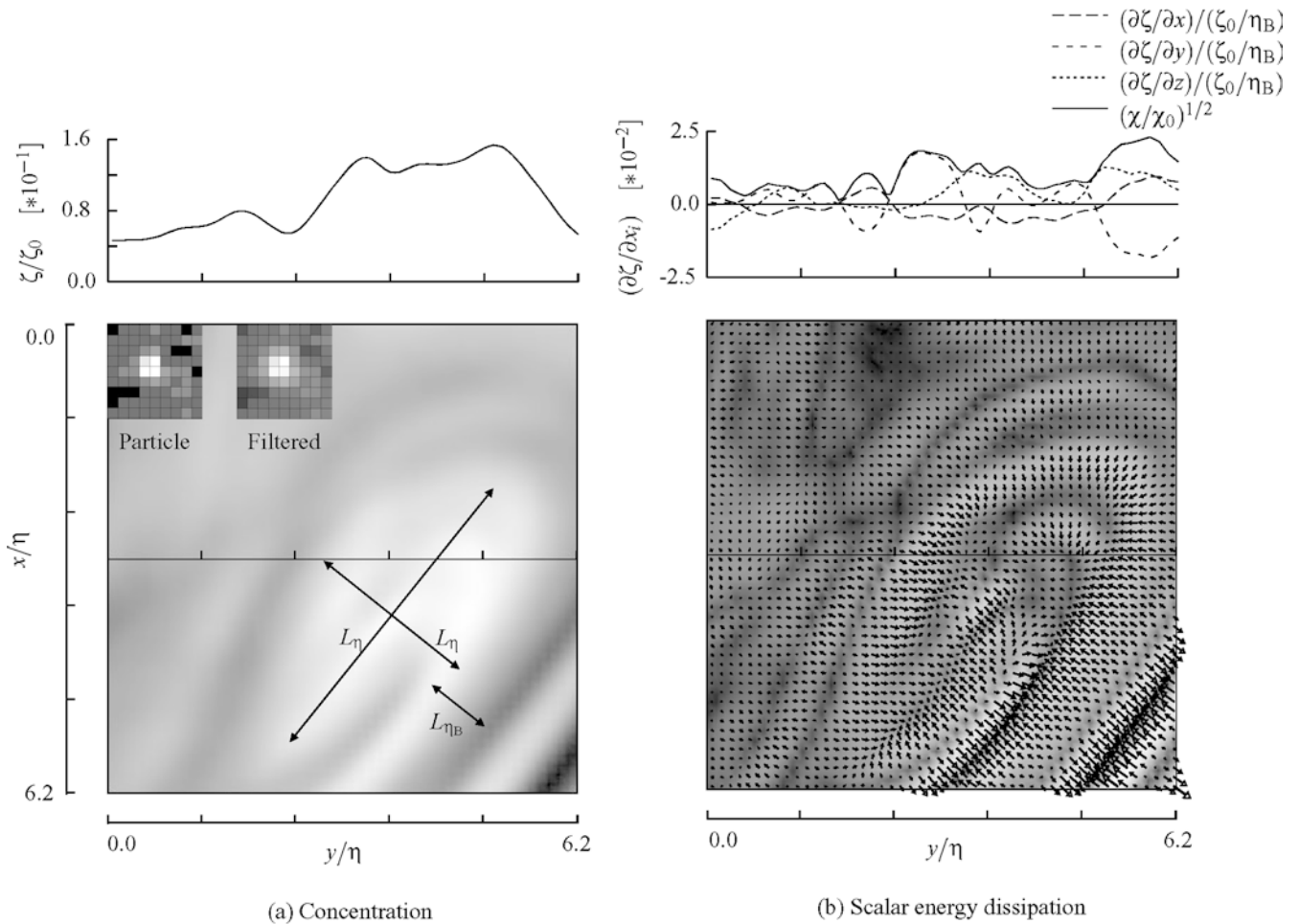

(a) Concentration

(b) Scalar energy dissipation

Fig. 18a, b. Enlargement of the concentration (**a**) and scalar energy dissipation (**b**) field of the white box shown in Fig. 16. The inset in (**a**) shows an image at the same resolution of a particle obtained from a focussing measurement. In the scalar energy dissipation field, the 2D projection of the gradient vectors are also depicted. The concentration and scalar gradient vector components along the (central) horizontal line are shown above the figures. The *arrows* in (**a**) depict some characteristic dimensions of the small-scale eddy

(a) Original data
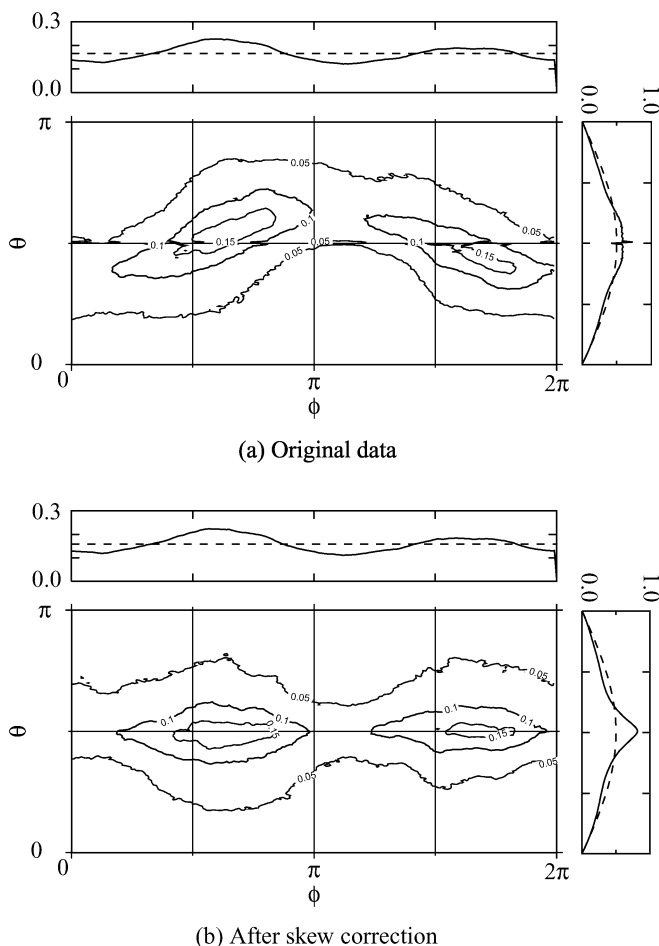

(b) After skew correction

Fig. 19a, b. Effect of the correction to the mean advection velocity on the joint pdf of the gradient vector spherical angles. The inclined orientation of the gradient vectors of the skewed concentration field is reflected by the waving tendency in the $\phi\theta$ joint pdf of the original data (**a**), and is corrected in the $\phi\theta$ joint pdf of the de-skewed data (**b**). The marginal pdfs of ϕ and θ shown above and to the right of the joint pdfs are compared with the distribution of a fully isotropic gradient vector field, indicated by the *dashed lines*
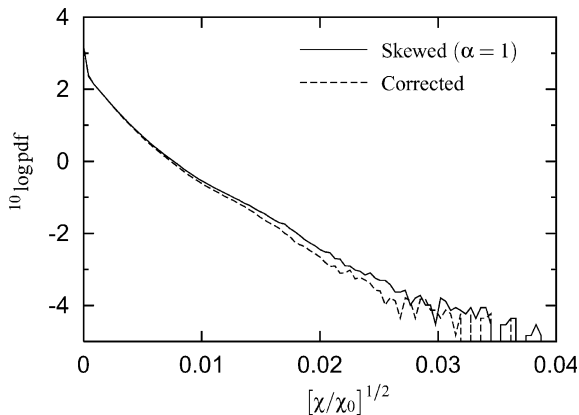

Fig. 20. Effect of the skew correction on the scalar energy dissipation distribution. A less intermittent scalar energy dissipation was found after the skew correction procedure

contribution in the measurement data, and is not related to the SED of the mixing scalar field. This is confirmed by the concentration-dissipation joint pdf shown in Fig. 22.

The low-valued SED peaks appear to be related to the small concentration values associated with the large area of the data volumes containing no fluorescent dye.

To obtain the marginal SED pdf without the noise contribution, the joint pdf is integrated in the ζ direction, starting from a threshold at $\zeta/\zeta_0=0.05$. Effectively, this implies that the SED is determined from those parts of the flow field containing only a signal level above the noise level. The resulting, bound marginal pdf of the SED is depicted by the dashed lines in Fig. 21. The bimodality of the pdf is removed, and the pdfs at both positions show a Gaussian-like signal peak only. In the right-hand graphs of Fig. 21, the same bound pdfs are depicted on a log scale and compared to a least-square fitted Gaussian distribution. This shows that the distributions are not fully Gaussian, but exhibit a slight negative skewness towards the small value for the SED. This observation corresponds to the measurement of many others, including for example, Su and Clemens (1999), who also found a negatively skewed $\log\chi$ distribution.

4.6
Downstream evolution of the mixing scalar field

4.6.1
Concentration distribution

Firstly, the downstream development of the concentration distribution shown in Fig. 23 is considered. The initial distribution closely downstream of the feed pipe (position p05 in Fig. 12a) extends over the whole signal range, indicating that, not only are areas of unmixed fluid with the initial concentration present, but also that quite some diffusion and back-mixing occurred. This was already anticipated in the qualitative analysis of the visualisation of the 3D data field, showing major parts of the dye structures with concentrations much smaller than the initial concentration. Further downstream at position p10, a gradual decay of the concentration distribution occurs. No unmixed dye structures (corresponding to ζ/ζ_0) are found downstream from $x/D_t=1.0$ (p10), where the dye leaves the centre plane in Fig. 12 (Sect. 4.1).

4.6.2
Scalar energy dissipation distribution

The bound marginal pdfs of $\log_{10}(\chi/\chi_0)$ are evaluated at all measurement positions, and their downstream evolution is plotted in Fig. 24. Since the SED is normalised with $\chi_0=\Gamma(\chi_0/\eta_B)^2$, the highest value, based on a grid spacing of $\Delta x \approx 5\eta_B$, that can be attained is $\log_{10}(\eta_B/\Delta x)^2 \approx -1.4$, corresponding to a difference between two neighbouring pixels of 255 grey values. At the first measurement position, p05, the largest value for the SED was found to be about -2.5 (corresponding to a difference between two neighbouring pixels of about 70 grey values). The highest value of -1.4 is not measured, probably due to the averaging effect of the Gaussian noise filter. This was anticipated in Fig. 18, illustrating a sharp image of a focused particle that was slightly smoothed over at the edges after noise filtering the image. Despite this slight degradation of spatial resolution, we expect that such high SED values at least have a very low probability of occurrence, since the
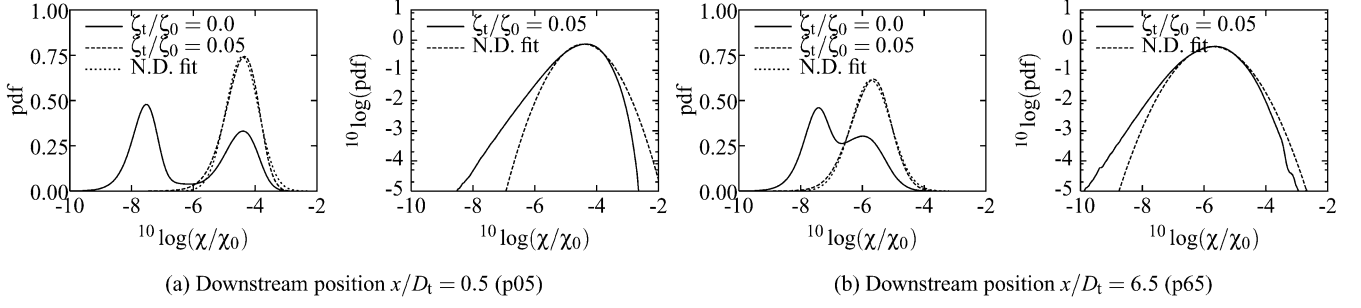
(a) Downstream position $x/D_t = 0.5$ (p05)

(b) Downstream position $x/D_t = 6.5$ (p65)

Fig. 21a, b. Distribution, $f_{\log \chi}$, of the scalar energy dissipation $\log_{10}(\chi/\chi_0)$ for a close (**a**) and a far downstream (**b**) position, put on a normal (*left*) and a logarithmic scale (*right*). On the *left*, a comparison is made between the unconditional and conditional marginal pdfs obtained from the joint pdfs depicted in Fig. 22. For the conditional pdf, a threshold on the concentration of $\zeta_t/\zeta_0 = 0.05$ is applied
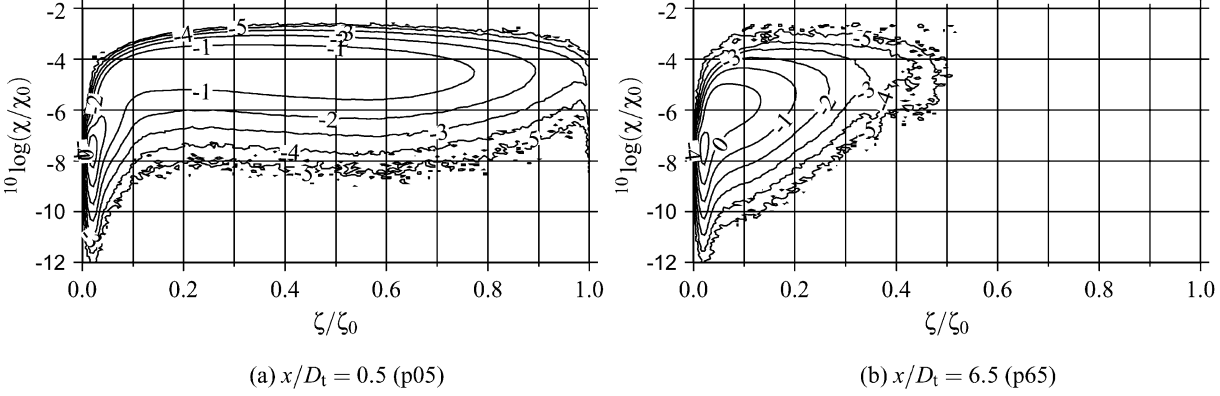

(a) $x/D_t = 0.5$ (p05)

(b) $x/D_t = 6.5$ (p65)

Fig. 22a, b. Joint concentration-dissipation pdf, $f_{\zeta \log \chi}$, obtained from the 3D concentration field measured at position $x/D_t = 0.5$ (**a**) and $x/D_t = 6.5$ (**b**), respectively. The number along the isocontours indicate the logarithmic values of the joint pdf

pdf smoothly runs to zero well before the high-end range is reached. This argument certainly applies for measuring positions further downstream, where the SED pdf is shifted to the left. Higher values of the SED, in principle, can be measured here (based on the values obtained at the first measuring position) but, apparently, these are just not present. This is indicative to a smoothly varying scalar field, with diffusion length scales larger than the spatial resolution. This agrees with the observations made in Sect. 4.3 (Fig. 18).

4.6.3
Mixing fraction

Together with the continuously decreasing trend of the maximum of the SED distribution, these distributions also tend to become wider, which is indicative to an increasing intermittent SED field (Kolmogorov 1962). The intermittency can also be quantified by the mixing fraction distribution[4] (see Fig. 25). The linear line corresponds to the mixing distribution of a fully homogeneous SED field. The mixing fraction of the scalar field shows the largest

increase for small volume fractions, indicating that a small fraction of the total volume takes care of a significant part of the total molecular scalar mixing. This is consistent with the observed thin layer-like structures of scalar energy dissipation that were found in the visualisation of a single 3D realisation shown in Fig. 14b.
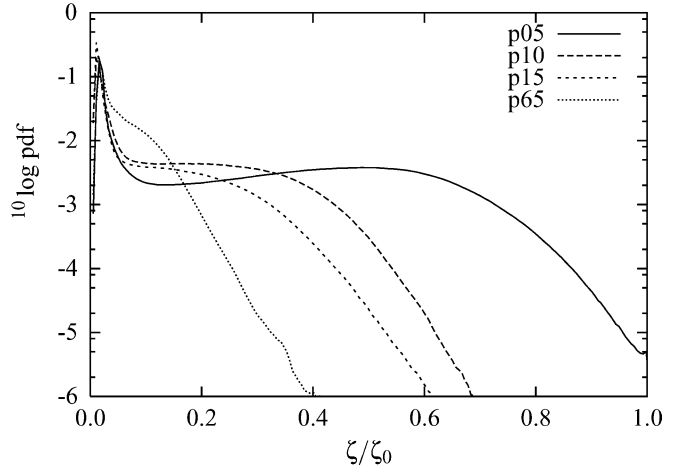

Fig. 23. Downstream evolution of the concentration pdfs. Positions p25–p55 are not shown since they are similar to p65

---

[4]The mixing fraction distribution is obtained from the SED pdf, $f_{\log \chi}$ (Fig. 24), by plotting the volume fraction $1 - \int_{-\infty}^{s=\chi} f_\chi(s) \, ds$ against the mixing fraction $1 - \frac{1}{\langle \chi \rangle} \int_{-\infty}^{s=\chi} s f_\chi(s) \, ds$, where the conditional distribution, f_χ, is obtained via the transformation $f_\chi = f_{\log(\chi)}/(\chi \ln(10))$.
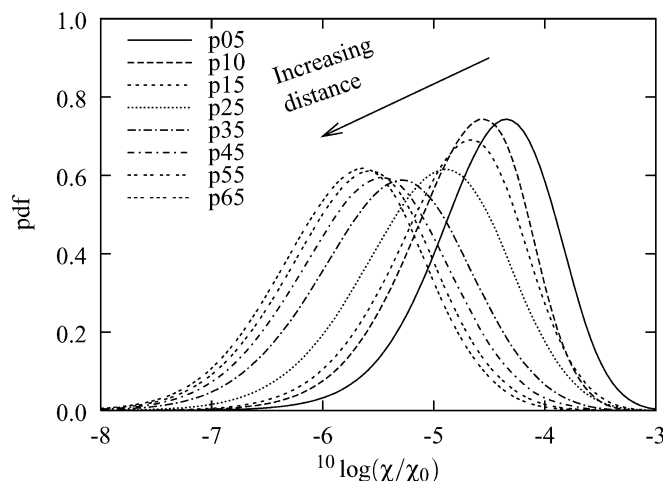
Fig. 24. Streamwise evolution of the conditioned pdfs of the scalar energy dissipation

Fig. 26. The downstream evolution of the M_{50} mixing fraction obtained from the mixing fraction distribution
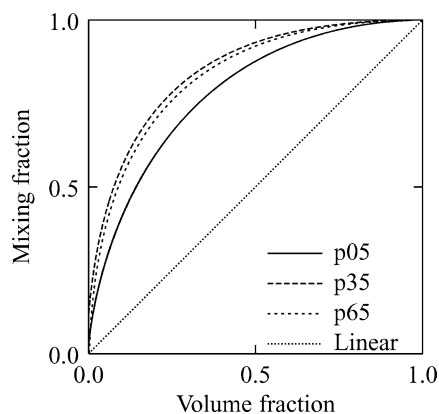

Fig. 25. Mixing fraction distribution at three downstream locations compared to the mixing fraction of a homogeneously distributed SED field

From the mixing fraction distribution, the M_{50} mixing fraction can be obtained, defined as the volume fraction taking care of 50% of the total scalar mixing. A wide pdf of $\log \chi$ corresponds to highly progressively increasing mixing fraction distribution and, as a consequence, corresponds to a small M_{50} mixing fraction The M_{50} mixing fractions are plotted in Fig. 26 for all downstream positions. Initially, the mixing fraction is decreasing from 0.15 toward 0.08 in the range $x/D_t=0.5\sim3.5$, while the last three measuring positions after $x/D_t=4.5$ show a slight increase again.

5
Discussion and conclusions

The ultimate goal in this paper was to extend the applicability of the 3D-LIF measuring technique to conserved, passive scalar mixing in a flow with significant advection velocity, in order to study the downstream development of the full scalar gradient vector field and its associated scalar energy dissipation in an industrial tubular reactor. This was achieved by increasing the spatial and temporal resolution by combining a high-speed CCD camera with a high-power Argon laser.
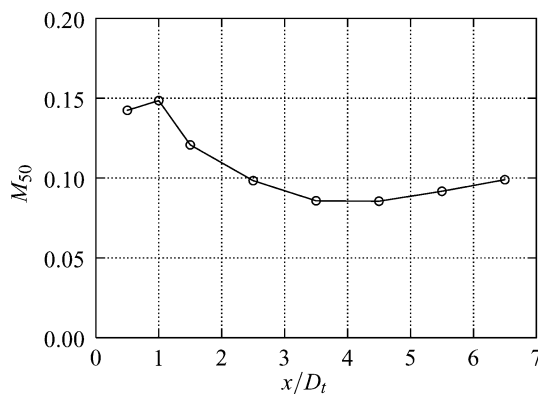
By means of a DNS, it was shown that a significant advection velocity skews the measured 3D scalar concentration field, resulting in a compression along the smallest eigenvectors of the skew tensor. As a result of this compression, the gradient vector field obtains a preferential direction, and an increasing intermittency of the SED is found. A correction method was proposed that applies a skew tensor with a deformation angle opposite to the one imposed by the instantaneous advection velocity. The advection velocity was estimated from the cross-correlation between two planes extracted from consecutive data volumes. It was shown that the correction can be successfully applied for a deformation angle in the range $\gamma=0\sim\pi/4$.

The 3D scalar concentration was measured at eight locations in the range $x/D_t=0.5\sim6.5$ downstream of the injector. The downstream evolution of the pdfs derived from the 3D-LIF data demonstrated that: (1) the high-end tail of the concentration pdf shows a fast decrease (Fig. 23), (2) the SED distribution is shifted to the lower-left SED range (Fig. 24) and (3) the mixing fraction initially is decreasing, while a slight increase is shown after about $4.5D_t$ (Figs. 25 and 26).

Based on our spatial resolution of $\Delta x \approx 5\eta_B$, it was expected that there would be at least a finite probability of measuring the maximum SED of $\log_{10}(\chi/\chi_0)=-1.4$. Instead, these values were approximately found (up to values as high as -2.5) at the first measuring position only, while further downstream, a much smoother scalar field seems to exist with much lower values for the SED. Also, based on visualisations of eddies of the size of the Kolmogorov scale (Fig. 18), scalar gradient length scales much larger than the spatial resolution seem to be very common. Although the average SED is decreasing, initially, a wider spread of the SED (and, by construction, a smaller mixing fraction) was found; evidence pointing to a more intermittent mixing scalar field.

The diffuse structures could not be related to an out-of-focus CCD camera, since particles of much smaller size are sharply depicted in the focusing of the camera, and, moreover, from the $\log \chi$ distribution, it was confirmed that smaller gradient length scales are actually measured, although with a much lower probability. Together with the fast decrease of the scalar concentration, this suggests that

dye structures are already efficiently mixed at short distances from the injector.

The macro scale transport of the tubular reactor may very well be responsible for the particular downstream evolution of the pdf distributions. It was shown by the 2D macro measurement (Fig. 12) that, in the complex flow of a tubular reactor, recirculation occurs and mixing is enhanced by both the wake and the turbulent jet. Moreover, an upwardly inclined jet was found due to the blockage promoted by the injector and, from $x/D_t=0.15$, the dye has already circulated along the tube walls. Due to the complex flow patterns, (a part of the) dye structures have a residence time much longer than expected from the advection time along a straight path from the injector, leading to better mixed dye structures.

Our observations suggest a unity proportionality constant in the relation, $\eta_B \approx Sc^{-1/2}\eta$, for the order estimate of the smallest diffusion length scales might be too strict. The Batchelor scale can be interpreted as the scalar diffusion length within one Kolmogorov eddy lifetime. In this interpretation, it is assumed that fully segregated dye from the fresh ambient fluid is released each eddy lifetime (e.g. Bakker and Van den Akker 1996). In reality, a continuous process of stretching and folding of small-scale eddies leads to mass exchange with its environment and also leads to a decrease in scalar differences and an increase in scalar diffusion length scales. Eventually, a homogeneous scalar composition is established with an "infinite" large scalar diffusion length scale.

In conclusion, the present paper demonstrated that 3D-LIF measurements in an industrial reactor are quite feasible. Compared to other 3D-LIF setups, both an increase in spatial and temporal resolution was achieved. Although a high-power illumination source was used to compensate for the decreasing LIF signal, the signal resolution of the 8-bit CCD camera may be too low to capture the full range of concentration values inherent in such intermittent flows. Using a camera with a larger bit-depth is desirable although, usually, this also degrades its temporal resolution. Alternatively, a laser sheet can be created from a fast-sweeping beam instead of forming it from a cylindrical lens. This enables us to form a more uniform sheet, with less high-frequency fluctuations, leading to lower noise levels in the fluorescent signal. A positive side effect is that the spatial resolution can also be improved, which allows us to validate the suggestion that the smallest diffusion length scales in this particular flow facility are larger than that given by the standard Batchelor estimate.

The SED that can be derived from the 3D scalar fields reveals in detail the turbulent mixing scalar field in the reactor. In particular, the development of intermittency is interesting, since this aspect is normally not very well captured in numerical simulations. Advanced sub-grid scale models should also be capable of predicting this. Measurements like these can contribute to the improvement and validation of models and numerical simulations of turbulent reactive scalar mixing in industrial reactors.

References

Bakker RA (1996) Micromixing in chemical reactors: Models, experiments and simulations. PhD thesis, Delft University of Technology

Bakker RA, Van den Akker HEA (1996) A Lagrangian description of micromixing in a stirred tank reactor using 1D-micromixing models in a CFD flow field. Chem Eng Sci 51(11):2643–2648

Baldyga J, Bourne JR (1984) A fluid mechanical approach to turbulent mixing and chemical reaction. Part 2: Micromixing in the light of turbulence theory. Chem Eng Commun 28:243–258

Brethouwer G (2001) Mixing of passive and reactive scalars in turbulent flows. PhD thesis, Delft University of Technology

Castleman KR (1979) Digital image processing. In: Openheim AV (ed) Prentice Hall signal processing series. Prentice-Hall, Englewood Cliffs, NJ

Colucci PJ, Jaberi FA, Givi P, Pope SB (1998) Filtered density function for large eddy simulation of turbulent reacting flows. Phys Fluids 10(2):499–515

Dahm WJA, Southerland KB, Buch KA (1990) Four-dimensional laser induced fluorescence measurements of conserved scalar mixing in turbulent flows. In: Proceedings of the 5th international symposium on applications of laser techniques to fluid mechanics, Lisbon, Portugal, July 1990

Dahm WJA, Southerland KB, Buch KA (1991) Direct, high resolution, four-dimensional measurements of the fine scale structures of Sc>>1 molecular mixing in turbulent flows. Phys Fluids A-Fluid 3(5):1115–1127

Derksen JJ, Van den Akker HEA (1999) Large eddy simulations on the flow driven by a Rushton turbine. AIChE J 45(2):209–221

Fox RO (1997) The Lagrangian spectral relaxation model of the scalar dissipation in homogeneous turbulence. Phys Fluids 9(8):2364-2386

Frank JB, Lyons KM, Long MB (1991) Technique for three-dimensional measurements of the time development of turbulent flames. Opt Lett 16(12):958–960

Hinze JO (1975) Turbulence, 2nd edn. McGraw-Hill, New York

Hoffmann A, Zimmerman F, Schultz C (2002) Instantaneous three-dimensional visualization of concentration distribution in turbulent flows with a single laser. In: Proceedings of the 1st international conference on optical and laser diagnostics, London, England, December 2002

Hopkins H (1955) The frequency response of a defocused optical system. P Roy Soc A 231:91–106

Knaus DA, Gouldin FC, Hinze PC, Miles PC (1999) Measurement of instantaneous flamelet normals and the burning rate in a SI engine. Technical report 1999–01–3543, SAE

Kolmogorov AN (1962) A refinement of previous hypotheses concerning the local structure of turbulence in a viscous incompressible fluid at high Reynolds number. J Fluid Mech 13:82–85

Landenfeld T, Kremer A, Hassel EP, Janicka J, Schäfer T, Kazenwadel J, Schultz C, Wolfrum J (1998) Laser-diagnostic and numerical study of strongly swirling natural gas flames. P Combust Inst 27:1023–1029

Maas HG, Stefanidis A, Gruen A (1994) From pixels to voxels: Tracking volume elements in sequences of 3-D digital images. In: ISPRS commission III: Intercongress symposium, Munich, Germany

Nygren J, Hult J, Richter M, Aldén M, Christensen M, Hultqvist A, Johansson B (2002) Three-dimensional laser-induced fluorescence of fuel distribution in a HCCI engine. P Combust Inst 29 (in press)

Overholt MR, Pope SB (1996) Direct numerical simulations of a passive scalar with imposed mean gradient in isotropic turbulence. Phys Fluids 8(11):3128–3148

Paul PH, Van Cruyningen I, Hanson RK, Kychahoff G (1990) High resolution digital flowfield imaging of jets. Exp Fluids 9:241–251

Prasad RR, Sreenivasan KR (1990) Quantitative three-dimensional imaging and the structure of passive scalar fields in fully turbulent flows. J Fluid Mech 27:507–521

Su LK, Clemens NT (1999) Planar measurements of the full three-dimensional scalar dissipation rate in gas-phase turbulent flows. Exp Fluids 27:507–521

Ten Cate A (2002) Turbulence and particle dynamics in dense crystal sluries. PhD thesis, Delft University of Technology

Van Vliet E, Derksen JJ, Van den Akker HEA (2000a) Four-dimensional laser induced fluorescence measurements of micro-mixing in a tubular reactor. In: Proceedings of the 10th European conference on mixing, Delft, July 2000

Van Vliet E, Derksen JJ, Van den Akker HEA (2000b) Measurements of micro-mixing in a tubular reactor using a four-dimensional laser induced fluorescence technique. In: Proceedings of the 10th international symposium on applications of laser techniques to fluid mechanics, Lisbon, Portugal, July 2000

Van Vliet E, Derksen JJ, Van den Akker HEA (2001) Modelling of parallel competitive reactions in isotropic homogeneous turbulence using a filtered density function approach for large eddy simulations. In: Proceedings of the 3rd international symposium on computational technologies for fluid/thermal/chemical systems with industrial applications, Atlanta, Georgia, USA, September 2001

Van Vliet E, Derksen JJ, Van den Akker HEA (2003) Turbulent reactive mixing in a tubular reactor: An LES/FDF approach. AIChE J (to be submitted)

Walker DA (1987) A fluorescence technique for measurement of concentration in mixing liquids. J Phys E Sci Instrum 20:217-224

Yip B, Lam JK, Winter M, Long MB (1987) Time resolved three-dimensional concentration measurements in a gas jet. Science 235:1209–1211

Yip B, Long MB (1986) Instantaneous planar measurements of the complete three-dimensional scalar gradient in a turbulent jet. Opt Lett 11:64–66